Editors' Suggestion

Chiral breakdown engineered by mesoscale Dzyaloshinskii-Moriya interaction in biaxial magnetic nanotubes

Kostiantyn V. Yershov [1,2,*] Svitlana Kondovych [1,†] and Denis D. Sheka [3,‡]

[1] *Institute for Theoretical Solid State Physics, Leibniz Institute for Solid State and Materials Research Dresden, D-01069 Dresden, Germany*

[2] *Bogolyubov Institute for Theoretical Physics of the National Academy of Sciences of Ukraine, 03143 Kyiv, Ukraine*

[3] *Taras Shevchenko National University of Kyiv, 01601 Kyiv, Ukraine*

(Received 13 February 2025; revised 8 April 2025; accepted 21 April 2025; published 15 May 2025)

Curvilinear geometries in magnetic nanostructures provide a unique platform for exploring the interplay among symmetry, topology, and curvature in magnetization dynamics. In this paper, we analytically study the static and dynamic properties of magnetic domain walls in biaxial magnetic nanotubes with intrinsic Dzyaloshinskii-Moriya interaction of different symmetries. We show that geometry-driven local and nonlocal interactions govern domain profiles and dynamics, enabling precise control over wall propagation and Walker breakdown field. Furthermore, the combination of bulk-type Dzyaloshinskii-Moriya interaction and curvature leads to chirality symmetry breaking and chiral breakdown in magnetic domain wall motion. These findings offer a framework for tailoring domain wall textures in cylindrical nanotubes, unlocking functionalities for advanced applications in curvilinear magnonics and data storage technologies.

DOI: 10.1103/PhysRevB.111.184419

I. INTRODUCTION

Domain walls (DWs) in ferromagnetic nanostructures represent a cornerstone of modern magnetism, with significant implications for spintronic and data storage technologies [1–6]. Ferromagnetic thin films [7–14], nanowires [15–20], and nanotubes [21–31] exhibit a wide variety of magnetic DW configurations, including Bloch and Néel walls, as well as more exotic hybrid textures driven by the Dzyaloshinskii-Moriya interaction (DMI) [32,33]. The specific properties of these DWs—such as their magnetization profile, stability, mobility, and chirality—are determined by the underlying geometry and interactions within the material, allowing for tailored functionalities in advanced applications.

The stabilization of magnetic DWs depends on a complex interplay of forces, with key contributions from exchange interactions, magnetic anisotropy, DMI, and magnetostatic (dipole-dipole) interactions. In particular, local intrinsic DMI induces nontrivial chiral spin textures, such as skyrmions and chiral DWs, while magnetostatics shapes the overall energy landscape altering the texture profile and influences their dynamics [34–38]. In confined systems, nonlocal dipole-dipole interactions can give rise to chiral structures even in the absence of DMI [35,36]. However, in thin-film geometries, magnetostatics merely contributes to the local magnetic anisotropy energy [39,40], thereby primarily affecting the DW width.

In systems with curvilinear geometries, curvature and topology offer numerous intriguing effects that enrich the magnetic texture scenery [41–43]. Curvature influences both the static and dynamic of magnetization textures. The most prominent manifestation of curvature-induced effects are topological patterning and geometric magnetochiral effects [44]. A paradigmatic example of curvature-induced effects is offered by magnetic nanotubes [21–31,45–47]. These structures have become experimentally accessible through advanced fabrication techniques [31,48,49] and offer an important platform for next-generation technologies, including magnetic sensors, memory elements, and spintronic devices [50]. Magnetic nanotubes offer enhanced stabilization and control over DWs, providing new degrees of freedom through geometry-induced effects on DMI, anisotropy, and magnetostatic contributions. For instance, pattern-induced chiral symmetry breaking can occur in nanotubes due to the dipole–dipole interaction: two energetically equivalent vortex DWs with opposite chiralities can exhibit different dynamic properties [22,24,26], leading to the suppression of Walker breakdown [51] and the Cherenkov-like radiation of magnons for fast DWs [21,52]. The nonlocal dipole-dipole interaction in the vortex state tube introduces effects in magnetization dynamics not present in flat systems of the same material, such as asymmetric spin-wave propagation [53,54]. The joint action of intrinsic DMI and geometry-governed exchange-driven DMI gives rise to mesoscale DMI providing different opportunities for geometrical manipulations of material responses [55]. In tubular geometry, mesoscale DMI becomes a source of a new type of inclined DWs [56,57] and high velocities of vortex DWs [27,29] in magnetic nanotubes subjected to magnetic fields and spin-polarized currents.

*Contact author: k.yershov@ifw-dresden.de

†Contact author: s.kondovych@ifw-dresden.de

‡Contact author: sheka@knu.ua

In this paper, we demonstrate the profound influence of curvature on the static and dynamic properties of DWs in biaxial magnetic nanotubes with intrinsic DMI of different symmetries. We establish that the interplay between bulk-type DMI and curvature results in chirality symmetry breaking, driven by a preferred combination of DW topological charge and helicity. In a vortex magnetic field, this causes a chiral breakdown in DW propagation, whereas in an axial magnetic field it defines the direction of the DW motion.

We further show that for nanotubes with interfacial-type DMI, the DW profiles and dynamics are governed by the geometry-induced competition between local and nonlocal effects. While this symmetry configuration restrains chiral effects, it allows for tailored control over the Walker limit in an external magnetic field.

II. MODEL OF A MAGNETIC NANOTUBE

We consider a ferromagnetic cylindrical tubular shell of constant thickness W and mean radius R, described by the curved surface $\boldsymbol{\varsigma}(x_1, x_2) = \boldsymbol{\gamma}(x_1) + x_2\hat{\boldsymbol{z}}$ with $\boldsymbol{\gamma} = R\cos(x_1/R)\hat{\boldsymbol{x}} + R\sin(x_1/R)\hat{\boldsymbol{y}}$, see Figs. 1(a) and 1(b). Here, x_1 and x_2 are curvilinear coordinates on the surface $\boldsymbol{\varsigma}$. The introduced parametrization $\boldsymbol{\varsigma}(x_1, x_2)$ induces Euclidean metric $g_{\alpha\beta} = \delta_{\alpha\beta}$ and the tangential basis $\boldsymbol{e}_\alpha = \partial_\alpha\boldsymbol{\varsigma}$, where $\boldsymbol{e}_1 = \partial_1\boldsymbol{\gamma}$ is the unit vector tangential to $\boldsymbol{\gamma}$ and $\boldsymbol{e}_2 = \hat{\boldsymbol{z}}$. The basis $\{\boldsymbol{e}_1, \boldsymbol{e}_2\}$ is orthonormalized, thus the unit surface normal is introduced as $\boldsymbol{e}_3 = \boldsymbol{e}_1 \times \boldsymbol{e}_2$. This is a particular case of the cylinder surface parametrization [56], which corresponds to the conventional cylindrical coordinate system.

Curvilinear properties of the surface $\boldsymbol{\varsigma}$ are completely determined by the only parameter: curvature $\kappa = 1/R$ of the curve $\boldsymbol{\gamma}$. We assume that the thickness W of the film is small enough to ensure that the magnetization $\boldsymbol{M}$ is uniform along normal direction $\boldsymbol{e}_3$ (coordinate x_3). The energy of such a magnetic tube we model with the following functional:

$$\mathcal{E}[\boldsymbol{m}] = \frac{E}{E_0} = \iint [\mathscr{E}_{\text{X}} + d\mathscr{E}_{\text{D}} + \mathscr{E}_{\text{A}}]\mathrm{d}\xi_1\mathrm{d}\xi_2 + \frac{\mathcal{E}_{\text{MS}}}{wQ}, \qquad (1)$$

where $\boldsymbol{m} = \boldsymbol{M}/M_{\text{s}}$, M_{s} is the saturation magnetization, $E_0 = K_{\text{a}}\ell^3 w$ with $K_{\text{a}} > 0$ being the easy-axial (along $\boldsymbol{e}_1$) anisotropy constant arising from sample growth [30,58], $\ell = \sqrt{A/K_{\text{a}}}$ is the characteristic length scale of the system (magnetic length), with A being exchange stiffness, $\xi_\alpha = x_\alpha/\ell$ are dimensionless curvilinear coordinates, $w = W/\ell$ is the dimensionless film thickness, $Q = 2K_{\text{a}}/(\mu_0 M_{\text{s}}^2)$ is the anisotropy quality factor of a material, and μ_0 is the magnetic permeability of vacuum. The first integral part on the right-hand side of (1) comprises the local energy terms. The first term in square brackets is energy density of the nonuniform exchange, $\mathscr{E}_{\text{X}} = -\boldsymbol{m}\cdot\nabla^2\boldsymbol{m}$. The second term corresponds to the DMI energy density $\mathscr{E}_{\text{D}}$, with $d = D/\sqrt{AK_{\text{a}}}$ being the dimensionless DMI constant. We consider two types of DMI: (i) $\mathscr{E}_{\text{D}}^b = \boldsymbol{m}\cdot[\nabla\times\boldsymbol{m}]$ is applicable for systems with T and O symmetries [59]. In the following this is called bulk-type DMI. (ii) $\mathscr{E}_{\text{D}}^i = -\boldsymbol{m}\cdot[(\boldsymbol{e}_3\times\nabla)\times\boldsymbol{m}]$ is valid for ultrathin films [7,60], bilayers [61], or materials belonging to C_{nv} crystal classes. In the following, we call this DMI of interfacial type. Here and below, indices b and i correspond to the bulk and interfacial DMI types, respectively. The third term in square brackets corresponds to the biaxial anisotropy $\mathscr{E}_{\text{A}} = 1 - (\boldsymbol{m}\cdot\boldsymbol{e}_1)^2 + \epsilon(\boldsymbol{m}\cdot\boldsymbol{e}_3)^2$ with anisotropy ratio $\epsilon = K_{\text{s}}/K_{\text{a}} > 0$, where K_{s} is the easy-surface anisotropy constant. The case with $\epsilon > 1$ corresponds to the nanotubes, experimentally studied by Josten *et al.* [30]. The last energy term in (1) describes the nonlocal magnetostatic energy due to dipole-dipole interactions, $\mathcal{E}_{\text{MS}} = \int \mathrm{d}\boldsymbol{\xi}\int \mathrm{d}\boldsymbol{\xi}'(\boldsymbol{m}(\boldsymbol{\xi})\cdot\nabla)(\boldsymbol{m}(\boldsymbol{\xi}')\cdot\nabla')|\boldsymbol{\xi}-\boldsymbol{\xi}'|^{-1}$.

In the following sections, we separately consider the two types of DMI, deriving the DW magnetization profiles that minimize energy functional (1) for each case, and then analyze the DW dynamics in an external magnetic field.

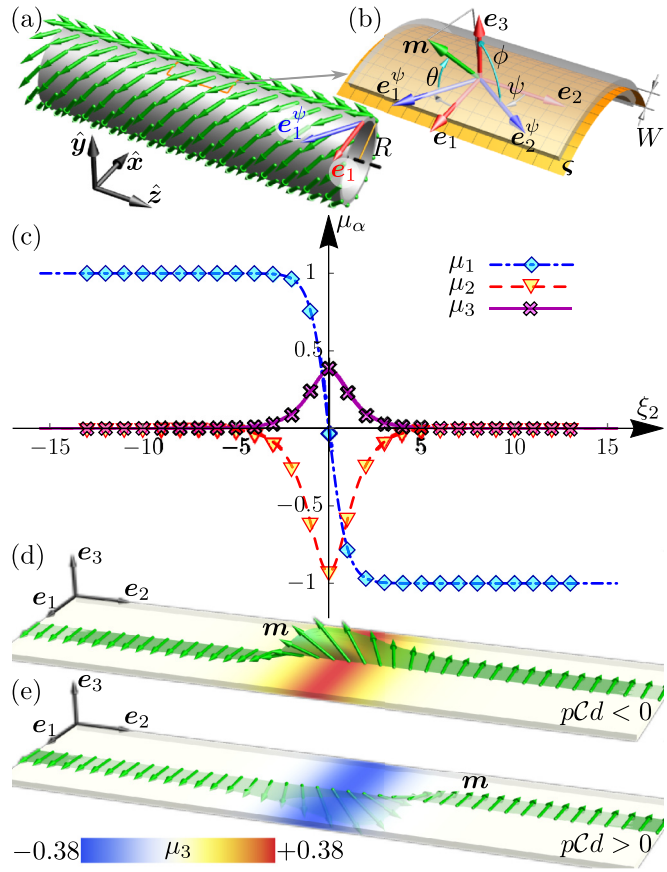

FIG. 1. Static domain walls in a cylindrical shell with bulk-type DMI. (a), (b) Schematic representation of a magnetic texture on a cylindrical tubular shell of mean radius R and thickness W. Magnetization $\boldsymbol{m}$ (green arrows) forms a tilted vortex state at equilibrium (a) and is parametrized by angles $\{\theta, \phi\}$ in ψ-rotated reference frame (b). (c) Numerical simulation results (symbols) for magnetization components μ_α in the rotated reference frame (2). Lines correspond to the analytical ansatz (5) with equilibrium DW profile parameters (7). Panel (d) illustrates the reconstructed magnetization distribution from (c) in an unrolled cylindrical shell with $pCd < 0$. Color scheme corresponds to the normal to the surface magnetization component μ_3. Green arrows show the DW magnetic texture, $\boldsymbol{m}(\xi_2)$, in which μ_3 is amplified (2 times) for visibility due to its small magnitude. Parameters used in numerical simulations are $p = 1$, $d = 0.25$, $\varepsilon = 0.5$, and $\varkappa = 0.2$, resulting in the tilt of $\boldsymbol{m}$ by a small angle $\psi \approx 0.025$. (e) DW with the opposite chirality, $pCd > 0$.

III. DOMAIN WALL ON A NANOTUBE WITH BULK-TYPE DMI

In the absence of DMI, the equilibrium magnetization texture forms a vortex state with $\boldsymbol{m}_{\rm v}(\xi_1) = \boldsymbol{e}_1$ [58]. Stabilized mainly by anisotropy K_a, the vortex state is favorable for $\varkappa < 2\sqrt{1+\varepsilon}/\pi$, see Appendix A. The symmetry of bulk-type DMI, $\mathscr{E}^b_{\rm D} = \boldsymbol{m}\cdot[\nabla\times\boldsymbol{m}]$, favors the emergence of the magnetization component m_3, normal to the surface of the nanotube. The DMI also inclines the magnetization, leading to the *tilted vortex state*, see Fig. 1(a). The direction of this deviation, determined by a tilt angle $\psi \approx -d\varkappa/2$, depends on the sign of DMI constant d, see Appendix B 1 for details. Note that the tilt is proportional to the dimensionless curvature $\varkappa = \ell/R$.

To parametrize the unit vector of magnetization, we first rotate the reference frame in the local rectifying surface by the angle ψ, as shown in Fig. 1(b). The magnetization in the rotated ψ frame $\{\boldsymbol{e}_1^\psi, \boldsymbol{e}_2^\psi, \boldsymbol{e}_3^\psi \equiv \boldsymbol{e}_3\}$ reads

$$\boldsymbol{m} = \mu_\alpha \boldsymbol{e}_\alpha^\psi = \cos\theta \boldsymbol{e}_1^\psi + \sin\theta\big(\cos\phi \boldsymbol{e}_2^\psi + \sin\phi \boldsymbol{e}_3\big), \tag{2}$$

where angular variables θ and ϕ depend on the spatial and temporal coordinates. In the following, m_α denote the components of vector $\boldsymbol{m}$ in the conventional cylindrical coordinate system, while μ_α correspond to the components of the same vector in the rotated reference frame. Using this reference frame, we diagonalize the effective anisotropy energy density of the cylinder (Appendix B 1). The total local energy density in the rotated frame of reference reads ($\{\alpha, \beta\} = \{1, 2\}$),

$$\begin{aligned}\mathscr{E}^b = {} & \partial_\alpha\mu_\beta\partial_\alpha\mu_\beta - \mathcal{K}_1^b\mu_1^2 + \mathcal{K}_3^b\mu_3^2 \\ & + \mathcal{D}_{\beta 3}^{b(\alpha)}(\mu_\beta\partial_\alpha\mu_3 - \mu_3\partial_\alpha\mu_\beta).\end{aligned} \tag{3}$$

Coefficient $\mathcal{K}_1^b$ characterizes the strength of the effective easy-axis anisotropy, while $\mathcal{K}_3^b$ gives the strength of the effective easy-surface anisotropy. The parameters $\mathcal{D}_{\beta 3}^{b(\alpha)}$ can be interpreted as mesoscale DMI coefficients [55]. In the case of small curvature and DMI strength, the effective anisotropy and DMI constants can be attributed to the geometrical parameters of the system,

$$\begin{aligned}&\mathcal{K}_1^b \approx 1 - \varkappa^2(1-d^2/2), \quad \mathcal{K}_3^b \approx \varepsilon + \varkappa^2(1-d^2/4),\\ &\mathcal{D}_{13}^{b(1)} \approx -2\varkappa + \varkappa d^2/2, \quad \mathcal{D}_{13}^{b(2)} \approx d,\\ &\mathcal{D}_{23}^{b(1)} \approx -d - d\varkappa^2, \quad \mathcal{D}_{23}^{b(2)} \approx \varkappa d^2/2.\end{aligned} \tag{4}$$

The nonlocal magnetostatic energy term in (1), $\mathcal{E}_{\rm MS}$, comprises the interactions between the surface, $\sigma^\pm = \pm m_3$, tangential, $\rho = -\partial_1 m_1 - \partial_2 m_2$, and geometrical, $g = -m_3/x_3$, magnetostatic charges [43]. In the considered tubular geometry, both anisotropy and magnetostatics favor a uniform tangential magnetization (competing with the DMI contribution), and thus it is only the DW region that is charged. The ψ rotation of the reference frame does not affect σ nor g since $\mu_3 = m_3$, and the tangential charge is rotation-invariant, $\rho = -\partial_1\mu_1 - \partial_2\mu_2$.

Here, we consider the thin-shell limit case, $w\varkappa \ll 1$, in which the leading contribution to magnetostatic energy comes from the surface charges and is local and linear in w. All other interactions are nonlocal and scale as higher order on the shell thickness w [39,40,62]. Moreover, the magnetic symmetry of terms corresponding to interactions $\mathcal{E}_{\rm MS}^{\rho-\rho}$, $\mathcal{E}_{\rm MS}^{g-g}$, and $\mathcal{E}_{\rm MS}^{\sigma-g}$ restricts symmetry breaking and cannot lead to chiral effects, resulting in a small correction of $\mathrm{o}(w)$ to the total energy. Based on these considerations, we include the local part of magnetostatic energy in the energy density (3) as $\mathcal{E}_{\rm MS}^{\sigma-\sigma} = w\iint \mu_3^2 {\rm d}\xi_1{\rm d}\xi_2$ (see Appendix B 3) by explicitly shifting the anisotropy coefficient in (4): $\varepsilon = \epsilon + Q^{-1}$. Further, we derive the possible static magnetization configurations by variation of the total energy functional with density (3), and discuss the remaining magnetostatic terms $\mathcal{E}_{\rm MS}^{\sigma-\rho}$ and $\mathcal{E}_{\rm MS}^{g-\rho}$ based on the symmetry of the obtained variational ansatz.

A. Static domain wall solution

The ground-state magnetization textures arising from the energy functional (1) with bulk-type DMI form two tilted vortices with $\cos\theta_{\rm tv} = C = \pm 1$, which correspond to the two possible directions of the vortex circulation: clockwise with $C = 1$ [see Fig. 1(a)] and counterclockwise with $C = -1$. The structure of a DW between two tilted vortices with opposite circulations can be described analytically with the following ansatz (see Appendix B 2):

$$\cos\theta_{\rm DW}^b = -p\tanh\frac{\xi_2}{\Delta}, \quad \phi_{\rm DW}^b = \Phi. \tag{5}$$

Here, $p = \pm 1$ is a topological charge of the DW, and $\Delta = 1/\sqrt{\mathcal{K}_1^b}$ is a DW width. In the absence of DMI, ansatz (5) with $\cos\Phi_0 = \mathcal{C} = \pm 1$ becomes an exact solution, see Appendix B 2. We now investigate the finite curvature effects on the magnetization distribution in DWs in nanotubes. We apply a variational approach by using (5) as a DW ansatz with the DW width Δ and initial phase Φ being the variational parameters. By substituting (5) into the energy density functional (3), accounting for the surface magnetostatic energy term and integrating over ξ_1 and ξ_2, we obtain

$$\frac{\mathcal{E}_{\rm DW}^b}{2\pi/\varkappa} = \frac{2}{\Delta} + 2\Delta\big[\mathcal{K}_1^b + \mathcal{K}_3^b\sin^2\Phi\big] + p\,\pi\,\mathcal{D}_{13}^{b(2)}\sin\Phi. \tag{6}$$

The first two terms on the right-hand side in (6) determine the competition of the nonuniform exchange and anisotropy contributions, while the third term originates from the mesoscale DMI and demonstrates the coupling between the DMI strength $\mathcal{D}_{13}^{b(2)}$, DW topological charge p, and helicity $\mathcal{C}$. By introducing the DW phase $\Phi = \Phi_0 + \tilde{\Phi}$, one can write the last term as $p\mathcal{C}\pi\mathcal{D}_{13}^{b(2)}\sin\tilde{\Phi}$. This term depends on the chirality of a DW, defined by the sign of the product $(p\mathcal{C}d)$.

With the variational ansatz (5), we can estimate the remaining nonlocal contributions to magnetostatic energy $\mathcal{E}_{\rm MS}^{\sigma-\rho}$ and $\mathcal{E}_{\rm MS}^{g-\rho}$, which favor the coupling between the normal magnetization component μ_3 and the gradient of the tangential component $\partial_2\mu_2$, potentially allowing for the chiral effects, such as dynamic chiral symmetry breaking effects observed in [22–24] and the static nonlocal chiral symmetry breaking effect observed in [63]. However, in the DW configuration on a nanotube with bulk-type DMI (Fig. 1), the components μ_2 and μ_3 have the same parity with respect to $\xi_2 \to -\xi_2$, so energy terms $\mathcal{E}_{\rm MS}^{\sigma-\rho}$ and $\mathcal{E}_{\rm MS}^{g-\rho}$ are the same for the DWs of different chiralities shown in Figs. 1(d) and 1(e) and Figs. 2(b) and 2(c). Since no nonlocal chiral effects are expected, and the

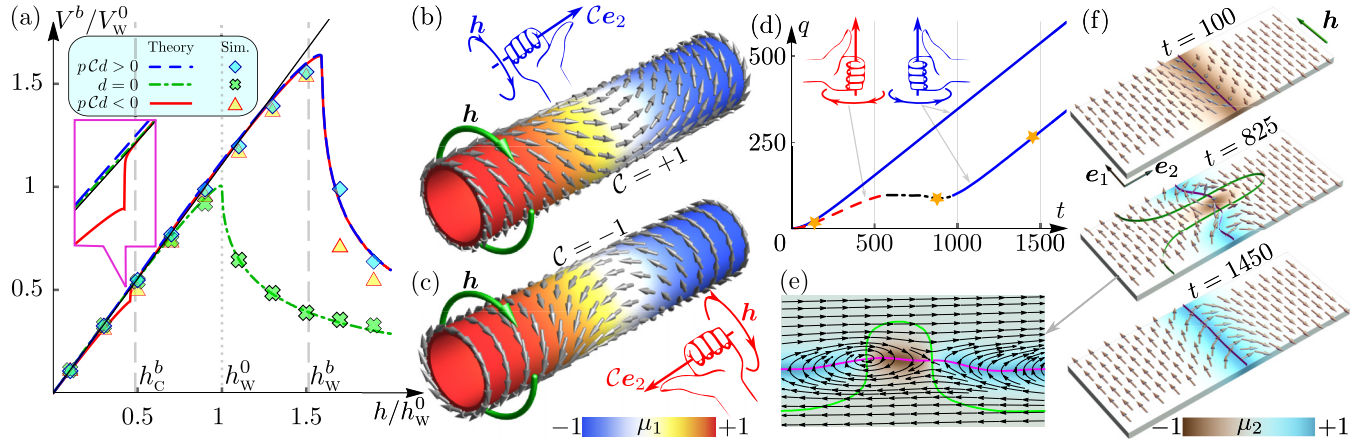

FIG. 2. DW motion in the applied vortex magnetic field in nanotubes with bulk-type DMI. (a) DW velocity V^b as a function of applied vortex magnetic field $\boldsymbol{h} = h\boldsymbol{e}_1$. Velocity is measured with respect to DMI-free Walker velocity V_W, and the value of the magnetic field is given in units of DMI-free Walker field h_W^0 (12) (dotted-vertical-light-gray line). Solid black line is the DW velocity in a traveling-wave regime (11a). Colored lines correspond to the numerical solution of the equations of motion (10). Dashed-vertical-light-gray lines mark the analytically predicted values for the chiral breakdown field h_C^b and Walker field h_W^b. The inset shows the enlarged area of the plot where the chiral breakdown occurs. Symbols correspond to the results of numerical simulations (Appendix D). Panels (b) and (c) schematically illustrate the DW structures of opposite helicities, $\mathcal{C} = \pm 1$, in nanotubes. The hand icons visualize the interplay between the DW helicity and the magnetic field: the thumbs point in the direction of $\mathcal{C}\,\boldsymbol{e}_2$, while the fingers curl along the orientation of the vortex field $\boldsymbol{h}$. (d) Time evolution of the DW position q for DWs of different helicities in the vortex magnetic field $h/h_W^0 = 0.7$, extracted from numerical simulations. Solid-blue lines correspond to the DW with favorable helicity, $\mathcal{C} = +1$ (b), dashed-red line to the DW with $\mathcal{C} = -1$ (c), and dash-dotted-black line indicates the transient stage. (e) Formation of a vortex-antivortex pair during the transient stage, shown by magnetization streamlines. (f) Snapshots of the magnetization texture in the unrolled nanotube before ($t = 100$), during ($t = 825$), and after ($t = 1450$) the DW helicity switching. Three time points are shown in (d) with orange stars. The middle snapshot captures the vortex-antivortex pair mediated breakdown shown in (e). Green and magenta lines in (f) and (e) correspond to isosurfaces with $\mu_1 = 0$ and $\mu_2 = 0$, respectively. Parameters used in simulations are $p = \pm 1$, $d = 0.25$, $\varkappa = 0.2$, $\eta = 0.01$, and $\varepsilon = 0.5$. Color schemes in (b) and (e), (f) correspond to the μ_1 and μ_2 components, respectively.

order of these energy terms is $\mathrm{o}(w)$ [39,40,62,64], we consider only the local surface magnetostatic contribution $\mathcal{E}_{\mathrm{MS}}^{\sigma-\sigma}$ as described above.

The minimization of (6) with respect to the DW width and phase results in the following equilibrium values:

$$\Delta_0^b = \sqrt{\frac{1}{\mathcal{K}_1^b} - \frac{1}{\mathcal{K}_1^b \mathcal{K}_3^b}\left[\frac{\mathcal{D}_{13}^{b(2)}}{d_0}\right]^2},$$

$$\sin\Phi_0^b = -p\,\frac{\mathcal{D}_{13}^{b(2)}}{d_0}\,\frac{\sqrt{\mathcal{K}_1^b/\mathcal{K}_3^b}}{\sqrt{\mathcal{K}_3^b - \left[\mathcal{D}_{13}^{b(2)}/d_0\right]^2}}, \tag{7}$$

where $d_0 = 4/\pi$ is the critical value of DMI that separates homogeneous and inhomogeneous magnetization textures in planar easy-axial systems [65]. The case of small curvature and DMI strength corresponds to $\Delta_0^b \approx 1 + [\varkappa^2 - \frac{(d/d_0)^2}{\varepsilon}]/2$ and $\Phi_0^b \approx \Phi_0 - p\mathcal{C}\frac{d}{d_0\varepsilon}$, valid for $d/d_0 < \varepsilon$. The comparison of these predictions with numerical simulations is in good agreement, see Fig. 1(c).

B. Domain wall dynamics in an external magnetic field

The interaction of a magnetic texture with an external magnetic field is described by the Zeeman energy density $\mathscr{E}_Z = -2\boldsymbol{h}\cdot\boldsymbol{m} = -2\boldsymbol{h}^\psi\cdot\boldsymbol{\mu}$, where $\boldsymbol{h} = \boldsymbol{H}/H_A$ is the normalized external magnetic field with $H_A = 2K_a/M_s$ being the anisotropy field.

To derive effective equations of DW motion, we use collective variable approach based on a $q - \Phi$ model [66]

$$\cos\theta_{\mathrm{DW}}^b = -p\tanh\frac{\xi_2 - q(t)}{\Delta}, \quad \phi_{\mathrm{DW}}^b = \Phi(t), \tag{8}$$

where q and Φ are time-dependent collective variables. Here and below, we consider dimensionless time measured in units of $\gamma_0 K_a/M_s$, where γ_0 is the gyromagnetic ratio.

1. The case of a vortex magnetic field

First, we consider the dynamics of DWs in a nanotube in a vortex magnetic field. The magnetic field is oriented in the tangential direction to the nanotube's surface, $\boldsymbol{h} = h\boldsymbol{e}_1$, which can be realized as an Ørsted field induced by a current flowing along the tube symmetry axis. In the rotated reference frame, $\boldsymbol{h}^\psi = h(\cos\psi\boldsymbol{e}_1^\psi - \sin\psi\boldsymbol{e}_2^\psi)$. By substitution of ansatz (5) into the Zeeman energy and integration over ξ_1 and ξ_2, we obtain

$$\frac{\mathcal{E}_Z^b}{2\pi/\varkappa} = -2h(2pq\cos\psi - \pi\Delta\cos\Phi\sin\psi). \tag{9}$$

Here, the first term ($\propto h\cos\psi$) pushes the DW along the tube axis, while the second term ($\propto h\sin\psi$) results in the deformation of the DW profile. However, in our case, we have $|\sin\psi| \approx |d\varkappa/2| \ll 1$, and as a result, we can neglect the dynamical changes of the DW width.

In terms of the collective variables, the equations of motion take the form (for details see Appendix B 4)

$$\frac{\eta}{\Delta}\dot{q} + p\,\dot{\Phi} = 2ph\cos\psi,$$
$$\dot{q} - \eta\Delta\dot{\Phi} = 2p\frac{\mathcal{D}_{13}^{b(2)}}{d_0}\cos\Phi + \mathcal{K}_3^b\Delta\sin 2\Phi - \pi h\Delta\sin\Phi\sin\psi. \quad (10)$$

Here, overdot denotes the time derivative with respect to dimensionless time, and η is the Gilbert damping parameter. The DW width is assumed to be a slave variable [67], i.e., $\Delta(t) = \Delta[\Phi(t)] = 1/\sqrt{\mathcal{K}_1^b + \mathcal{K}_3^b\sin^2\Phi^b}$. The behavior of the DW width is discussed in detail in Appendix B 4.

The set of equations (10) has a traveling-wave regime with $\dot{q} = V^b = \text{const}$ and $\dot{\Phi}^b = 0$. The corresponding DW velocity and phase are

$$V^b = 2p\frac{h\,\Delta_0^b}{\eta}\cos\psi \approx 2\frac{p\,h}{\eta}\left[1 + \frac{1}{2}\left(\varkappa^2 - \frac{1}{\varepsilon}\frac{d^2}{d_0^2}\right)\right], \quad (11a)$$

$$\Phi^b \approx \Phi_0^b + \frac{h}{\eta\varepsilon}\left[1 - \frac{\varkappa^2}{\varepsilon} + \frac{d}{d_0\varepsilon}\left(\frac{d}{d_0\varepsilon} - \mathcal{C}h\varkappa\right)\right]. \quad (11b)$$

The resulting DW velocity (measured with respect to the DMI-free Walker velocity $V_{\rm w} = (\varepsilon + \varkappa^2)\sqrt{2}/\sqrt{2 + \varepsilon - \varkappa^2}$) as a function of the applied field is presented in Fig. 2(a). The traveling-wave solution exists for the fields $h < h_{\rm w}^b$, where

$$h_c^b \approx h_{\rm w}^0 + p\,\mathcal{C}\frac{\eta}{\sqrt{2}}\frac{d}{d_0}, \quad h_{\rm w}^0 = \frac{\eta}{2}(\varepsilon + \varkappa^2). \quad (12)$$

Here, $h_{\rm w}^0$ is the Walker field for a DMI-free biaxial ferromagnetic nanotube. Estimated experimental values and typical time evolution of the parameters are given in Appendixes B and D.

For a fixed DW topological charge and a sign of DMI strength [e.g., for $\text{sign}(pd) = +1$] we can introduce two critical fields, namely: Walker field $h_{\rm w}^b = h_{\rm w}^0 + \eta d/(\sqrt{2}d_0)$ for a DW with $\mathcal{C} = +1$, Fig. 2(b) and chiral field $h_{\rm c}^b = h_{\rm w}^0 - \eta d/(\sqrt{2}d_0)$ for a DW with $\mathcal{C} = -1$, Fig. 2(c). The chiral field acquires two distinctive features: (i) at $h < h_{\rm c}^b$ the "unfavorable" DW helicity $\mathcal{C} = -1$ has lower average velocity than for the opposite helicity, see Fig. 2(a); (ii) at $h_{\rm c}^b < h < h_{\rm w}^b$ the average velocity is the same for both initial helicities because after the transient stage only one helicity survives, i.e., we have the traveling-wave motion with a single flip of the phase with $\Phi^b \to \Phi^b + \pi$. Movies within the Supplemental Material [68] capture the dynamics of DWs with different helicities. During the transient stage, marked in Fig. 2(d) with black-dashdotted lines, the DW with "unfavorable" helicity slows down during the phase flip and subsequently moves at a constant velocity. The DW helicity switching mechanism, illustrated by snapshots of simulated configuration in Fig. 2(f), occurs through the nucleation of vortex-antivortex pairs [Fig. 2(e) and the middle snapshot in Fig. 2(f)], followed by their annihilation, akin to the process described for vortex DWs in [23]. The origin of the vortex-antivortex pair generation is the nonlinear resonance of magnon modes with nonlinear coupling, the process originally studied for the planar vortex dynamics [69,70]. Finally, at $h > h_{\rm w}^b$ we see a sudden drop in the average DW velocity, see Fig. 2(a), which is typical for Walker breakdown. Here, both helicities periodically transform into each other as they propagate, showing periodic oscillations over the tube axis, so that the resulting average velocity is independent of the helicity.

The chirality-assisted DW behavior shown in Fig. 2 resembles the dynamics of head-to-head (tail-to-tail) vortex DWs in magnetic nanotubes studied in [22–24] and reflects geometry-induced chirality symmetry breaking. However, unlike the referenced studies, which focus on DMI-free systems where chiral symmetry breaking originates nonlocally from magnetostatic interactions, here we observe a local chiral effect, arising from the interplay between bulk-type DMI and curvilinear geometry.

2. The case of an axial magnetic field

Next, we study the dynamics of DWs in a nanotube with an external magnetic field oriented along the tube axis, i.e., $\boldsymbol{h} = h\boldsymbol{e}_2$, or, in the rotated frame of reference, $\boldsymbol{h}^\psi = h(\sin\psi\boldsymbol{e}_1^\psi + \cos\psi\boldsymbol{e}_2^\psi)$. Note that here we consider magnetic fields below the Walker field ($h \ll h_{\rm w}$). By substitution of ansatz (5) into the Zeeman energy and integration over ξ_1 and ξ_2 we obtain

$$\frac{\mathcal{E}_{\rm Z}^b}{2\pi/\varkappa} = -2h(2pq\sin\psi + \pi\Delta\cos\Phi\cos\psi). \quad (13)$$

Here, similarly to the case of the vortex field, we also have one term that pushes the DW ($\propto h\sin\psi$) and one that deforms the DW profile ($\propto h\cos\psi$). In this case, we restrict ourselves to the case of weak fields $h \ll h_{\rm w}^0$, in order to avoid dynamical deformations of the DW profile.

In terms of the collective variables, the equations of motion take the form (for details see Appendix B 4)

$$\frac{\eta}{\Delta}\dot{q} + p\,\dot{\Phi} = 2ph\sin\psi,$$
$$p\dot{q} - \eta\Delta\dot{\Phi} = 2p\frac{\mathcal{D}_{13}^{b(2)}}{d_0}\cos\Phi + \mathcal{K}_3^b\Delta\sin 2\Phi + h\pi\Delta\sin\Phi\cos\psi. \quad (14)$$

This set of equations has a traveling-wave regime with $\dot{q} = V^b = \text{const}$ and $\dot{\Phi}^b = 0$,

$$V^b = 2p\frac{h\Delta_0^b}{\eta}\sin\psi \approx -p\frac{d\varkappa}{\eta}h, \quad (15a)$$

$$\Phi^b \approx \Phi_0^b + \frac{hd}{2\varepsilon(2\mathcal{C}h + \varepsilon d_0)}\left(p\pi - \frac{d_0\varepsilon\varkappa}{\eta}\right). \quad (15b)$$

From (15) we can see that a DW has a finite velocity, and the direction of the DW motion is defined by the sign of product of the DW topological charge p, and DMI strength d, see Fig. 3. The finite velocity (15a) in an axial magnetic field is possible by the joint action of bulk-type DMI and curvature. In this case, the magnetization in the equilibrium state deviates from the easy-axis direction, and $\boldsymbol{h}\cdot\boldsymbol{m}_{\rm tv} = Ch\sin\psi \neq 0$.

IV. DOMAIN WALL ON A NANOTUBE WITH INTERFACIAL-TYPE DMI

In contrast to the case of bulk-type DMI discussed in Sec. III, the symmetry of interfacial-type DMI, $\mathscr{E}_{\rm D}^i = -\boldsymbol{m}\cdot[(\boldsymbol{e}_3\times\nabla)\times\boldsymbol{m}]$, follows the in-surface easy direction $\boldsymbol{e}_1$;

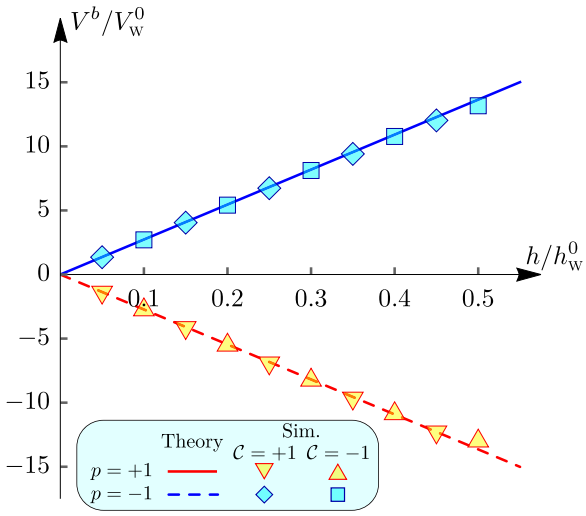

FIG. 3. DW motion in an axial magnetic field in nanotubes with bulk-type DMI. DW velocity V^b is plotted as a function of applied axial magnetic field $\boldsymbol{h} = h\boldsymbol{e}_2$. Velocity is measured in units of DMI-free Walker velocity $V_{\rm w}$, and the magnetic field is given in units of DMI-free Walker field, $h_{\rm w}^0$. Lines correspond to the traveling-wave regime of motion (15a) for DWs of different topological charge, $p = \pm 1$, while symbols correspond to the results of numerical simulations (Appendix D), where we use $p = \pm 1$, $d = 0.25$, $\varkappa = 0.2$, $\eta = 0.01$, and $\varepsilon = 0.5$.

therefore, the equilibrium magnetization texture forms one of two possible vortex states, $\boldsymbol{m}_{\rm v} = C\boldsymbol{e}_1$ with $C = \pm 1$, see Fig. 4(a). In this case, the unit vector of magnetization can be parametrized with angular variables (Θ, Φ) as shown in Fig. 4(b),

$$\boldsymbol{m} = \cos\Theta\boldsymbol{e}_1 + \sin\Theta(\cos\Phi\boldsymbol{e}_2 + \sin\Phi\boldsymbol{e}_3), \tag{16}$$

where Θ and Φ depend on the spatial and temporal coordinates.

The energy density for a nanotube with interfacial DMI can be written in the form, which is similar to the case of the bulk-type DMI (3),

$$\begin{aligned}\mathscr{E}^i = {} & \partial_\alpha m_\beta \partial_\alpha m_\beta - \mathcal{K}_1^i m_1^2 + \mathcal{K}_3^i m_3^2 \\ & + \mathcal{D}_{\beta 3}^{i(\alpha)}(m_\beta \partial_\alpha m_3 - m_3 \partial_\alpha m_\beta),\end{aligned} \tag{17}$$

with effective anisotropy and mesoscale DMI constants

$$\begin{aligned}&\mathcal{K}_1^i = 1 - \varkappa^2, \quad \mathcal{K}_3^i = \varepsilon + \varkappa(\varkappa + d),\\ &\mathcal{D}_{13}^{i(1)} = -(d + 2\varkappa), \quad \mathcal{D}_{13}^{i(2)} = 0,\\ &\mathcal{D}_{23}^{i(1)} = 0, \quad \mathcal{D}_{23}^{i(2)} = -d.\end{aligned} \tag{18}$$

Here, we have only two nonzero mesoscale DMI terms due to similar symmetry of both intrinsic interfacial and geometry-governed DMI.

We take into account the nonlocal magnetostatic energy terms in the same way as we did in Sec. III for the case of bulk-type DMI. We directly include the local part coming from the surface energy $\mathcal{E}_{\rm MS}^{\sigma-\sigma}$ by shifting the anisotropy ratio, $\varepsilon = \epsilon + Q^{-1}$, which appears in the effective anisotropy constant $\mathcal{K}_3^i$ in (18). The contributions from nonlocal magnetostatic terms potentially allowing for chiral effects,

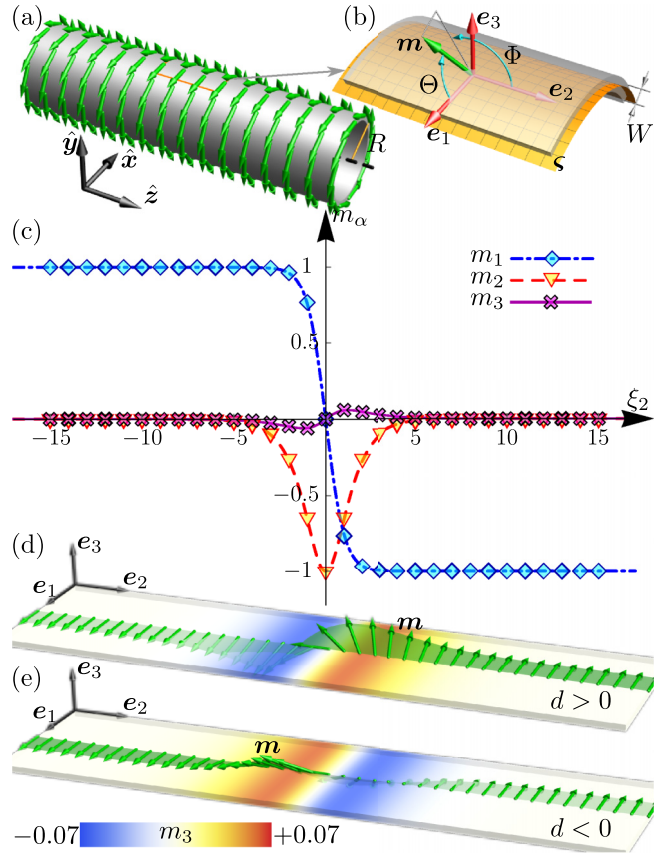

FIG. 4. Static domain walls in a cylindrical shell with interfacial-type DMI. (a), (b) Model of a cylindrical nanotube of mean radius R and thickness W with a magnetic texture. Magnetization unit vector $\boldsymbol{m}$ (green arrows) forms a vortex state at equilibrium (a) and is parametrized by angles $\{\Theta, \Phi\}$ in the curvilinear reference frame (b). (c) Numerical simulation results (symbols) for magnetization components m_α. Lines correspond to the analytical ansatz (19) with equilibrium DW profile parameters (21). (d) Reconstructed magnetization distribution from (c) in an unrolled cylindrical shell with $d > 0$. Color scheme corresponds to the normal to the surface magnetization component m_3. Green arrows show the DW texture $\boldsymbol{m}(\xi_2)$, in which m_3 is amplified (10 times) for illustrative purpose due to its small magnitude. In numerical simulations we set $p = +1$, $d = 0.25$, $\varepsilon = 0.5$, and $\varkappa = 0.2$. (e) DW profile with the opposite sign of DMI constant, $d < 0$.

$\mathcal{E}_{\rm MS}^{\sigma-\rho}$ and $\mathcal{E}_{\rm MS}^{g-\rho}$, we discuss further after the derivation of variational DW ansatz.

A. Static domain wall solution

The structure of a DW in a nanotube with interfacial-type DMI between two vortices with opposite circulations $\cos\Theta_{\rm v} = C = \pm 1$ with opposite circulations can be described analytically as (see Appendix C 1)

$$\cos\Theta_{\rm DW}^i = -p\tanh\frac{\xi_2}{\Delta}, \quad \Phi_{\rm DW}^i = \Phi_0 + a\frac{\xi_2}{\Delta}, \tag{19}$$

where a is a phase slope, and Δ is a DW width.

To study the finite curvature effects on the magnetization distribution in DWs, we apply a variational approach by using (19) as a DW Ansatz with the DW width Δ, initial phase

Φ_0, and phase slope a being the variational parameters. By inserting Eq. (19) into the energy density functional (17) and integrating over the ξ_1 and ξ_2, we obtain (see Appendixes C 1 and C 2)

$$\frac{\mathcal{E}^i_{\rm DW}}{2\pi/\varkappa} = \frac{2}{\Delta}\left(1+a^2\right) + 2a\mathcal{D}^{i(2)}_{23} - a\Delta\frac{\pi w\varkappa}{4Q} + \Delta\left[2\mathcal{K}^i_1 + \mathcal{K}^i_3\left(1-\pi a\frac{\cos 2\Phi}{\sinh(\pi a)}\right)\right]. \quad (20)$$

The minimization of (20) with respect to the DW width, phase, and its slope results in the following equilibrium values (approximation of a small phase slope):

$$\Delta^i_0 \approx 1/\sqrt{\mathcal{K}^i_1}, \quad \cos\Phi^i_0 = \mathcal{C} = \pm 1,$$
$$a^i_0 \approx -\frac{8\mathcal{D}^{i(2)}_{23}\sqrt{\mathcal{K}^i_1} - \pi w\varkappa/Q}{16\left(\mathcal{K}^i_1 + c\mathcal{K}^i_3\right)}, \quad c = \pi^2/12. \quad (21)$$

In the limit case of small curvature and DMI strength, $\Delta^i_0 \approx 1+\varkappa^2/2$ and $a^i_0 \approx [d+\pi w\varkappa/(8Q)]/(2+2c\varepsilon)$. The comparison of these predictions with numerical simulations confirms our analytical calculations, see Fig. 4. Note that we do not observe the tilt (with respect to the nanotube's axis) of the DW profile reported in the preprint by Josten *et al.* [30]. Both analytical calculations and numerical (spin-lattice and full-scale micromagnetic) simulations predict DWs perpendicular to the tube's axis.

Note that in the case of interfacial-type DMI, the magnetostatic contribution manifests not only as a shift in the anisotropy constant but also through the terms $\propto w\varkappa/Q$ in (20) and (21). These terms, arising from the interactions $E^{g-\rho}_{\rm MS}$ and $E^{\sigma-\rho}_{\rm MS}$, lead to the emergence of a DW configuration with a favorable sign of phase slope a^i_0, determined by the interplay between local and nonlocal contributions (see details in Appendix C 2). Importantly, the DW topological charge $p = \pm 1$ has no impact on the magnetostatic energy in the studied system, meaning chiral effects are absent. The preferred phase slope a^i_0 remains the same regardless of p or the helicity $\mathcal{C}$.

B. Domain wall dynamics in an external magnetic field

In order to derive effective equations of the DW motion, we use the collective variable approach based on a generalized $q-\Phi$ model [12],

$$\cos\Theta^i_{\rm DW} = -p\tanh\frac{\xi_2 - q(t)}{\Delta}, \quad \Phi^i_{\rm DW} = \Phi(t) + a\frac{\xi_2 - q(t)}{\Delta}. \quad (22)$$

For the case of interfacial-type DMI, we consider the dynamics of DWs in a nanotube only in a vortex magnetic field, i.e., $\boldsymbol{h} = h\boldsymbol{e}_1$. For the case of $\boldsymbol{h}\|\boldsymbol{e}_2$, DWs are *immobile* since $\boldsymbol{h}\cdot\boldsymbol{m} = 0$ in the ground state. By substitution of the ansatz (22) into the Zeeman energy and integration over ξ_1 and ξ_2 coordinates, we obtain the energy term that corresponds to the Zeeman energy density (9) with $\psi = 0$.

In terms of the collective variables, the equations of motion take the form

$$\eta\frac{\dot q}{\Delta} + (p - a\eta)\dot\Phi = 2ph,$$
$$(p+a\eta)\dot q - \eta\Delta\dot\Phi = \mathcal{K}^i_3\Delta\sin 2\Phi. \quad (23)$$

The DW width Δ, and phase slope a, are assumed to be slave variables, i.e., $\Delta^i[\Phi^i(t)] = 1/\sqrt{\mathcal{K}^i_1 + \mathcal{K}^i_3\sin^2\Phi^i}$ and $a^i[\Phi^i(t)] = (\frac{\pi w\varkappa}{8Q}\Delta^i - \mathcal{D}^{i(2)}_{23})\Delta^i/[2+2c(\Delta^i)^2\mathcal{K}^i_3\cos 2\Phi^i]$. The behavior of the DW width and phase slope is discussed in detail in Appendix C 3.

The set of equations of motion (23) has a traveling wave solution with

$$V^i = 2p\frac{h\Delta^i_0}{\eta}, \quad \Phi^i = \Phi^i_0 + \frac{p}{2}\arcsin\frac{h}{h^i_{\rm w}}, \quad (24)$$

with the Walker field

$$h^i_{\rm w} \approx h^0_{\rm w} + d\frac{\eta}{2}\left[\varkappa + p\frac{\varepsilon\eta}{2\sqrt{1+\varepsilon/2}}\right] + p\frac{\varepsilon\eta^2\varkappa}{2+\varepsilon}\frac{\pi w}{16Q}. \quad (25)$$

Estimated experimental values of the parameters and their typical time evolution, as well as Walker field dependence on curvature and DMI strength, are provided in Appendixes C and D. The Walker field (25) for a DW in a nanotube with interfacial-type DMI exhibits a linear shift with respect to the DMI strength d, as seen from the second term on the right-hand side, which arises from local interactions. While it contains the DW topological charge p, reasonable values of the damping constant $\eta \sim 10^{-2}$ render the p-term negligibly small compared to the curvature $\varkappa$. The same reasoning applies to the magnetostatics-generated last term in (25). We conclude that the DW motion does not exhibit chiral effects in the considered setup, and the shift in the Walker field depends solely on the sign of the DMI strength (see Fig. 5). Moreover, the Walker field shift is weaker here compared to the case with bulk-type DMI (Sec. III B 1), being quadratic with respect to small parameters $\propto \varkappa d$, while for the bulk-type DMI, the leading term in the field shift (12) scales linearly on the order of d.

V. CONCLUSIONS

The effects of DMI and curvature on the statics and field-driven DW motion are analyzed using cylindrical biaxial magnetic nanotubes as a model system. The results demonstrate that the presence of DMI leads to specific deformations in the DW profile, with the pattern and magnitude of these distortions dictated by the DMI type and strength, respectively. In particular, bulk-type DMI generates a symmetric normal (out-of-surface) magnetization component (Fig. 1), whereas interfacial-type DMI induces asymmetric distortions in the normal magnetization component (Fig. 4).

The joint action of curvature and bulk-type DMI results in a tilting of the vortex ground state of magnetization by an angle $\psi \propto \varkappa d$ as compared to the DMI-free case. This effect enables the translational motion of a DW with constant velocity $V^b/h \propto \varkappa d$ in an axial magnetic field. Moreover, in the case of a vortex magnetic field, bulk-type DMI leads to the appearance of the preferable combination of DW topological charge and helicity, $\mathrm{sign}(p\mathcal{C}d) < 0$. The latter effect induces chirality breaking in DW motion: a DW with nonpreferable chirality undergoes a vortex-antivortex pair mediated breakdown before settling into motion at a constant velocity, as shown in Figs. 2(d)–2(f). Additionally, bulk-type DMI in-

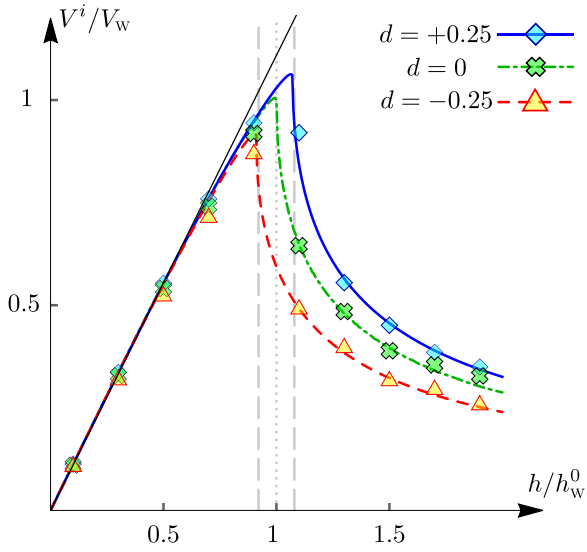

FIG. 5. Domain wall motion in nanotubes with interfacial-type DMI in the applied vortex magnetic field $\boldsymbol{h} = h\boldsymbol{e}_1$. DW velocity V^i is measured with respect to DMI-free Walker velocity V_w, and the magnetic field value is given in units of DMI-free Walker field h_w^0 (dotted-vertical-gray line). The solid-black line illustrates the traveling wave regime (24). Colored lines show the numerical solution of the equations of motion (23). Dashed-vertical-gray lines mark the predicted values of the Walker field (25) for different signs of DMI strength d. Symbols correspond to the results of numerical simulations (Appendix D) with $p = +1$, $d = \pm 0.25$, $\varkappa = 0.2$, $\eta = 0.01$, and $\varepsilon = 0.5$.

creases the Walker field proportionally to the DMI constant, thereby extending the range of applied fields that enable steady DW motion.

In systems with interfacial-type DMI, the Walker field also exhibits a linear shift with respect to the DMI strength; however, this effect is weaker than in the bulk-type DMI case, and no chiral breakdown in DW motion is observed. Notably, the asymmetry of the static DW profile in this case is jointly tuned by DMI and magnetostatics, where the latter contributes in the thin-film limit to both effective anisotropy and DMI constants. Nonlocal interactions, however, do not generate chiral effects in the DW dynamics and eventually result in a minor additional shift in the Walker field.

The synergy between symmetry and geometry in magnetic nanotubes provides an enhanced toolkit for exploring topological effects and features of curvilinear magnetization dynamics. Our predictions pave the way for tailoring the properties of DW textures in thin cylindrical nanotubes, enabling their use as critical components in nanoelectronic devices.

ACKNOWLEDGMENTS

We thank Ulrike Nitzsche for technical support. This work was financed in part via the German Research Foundation (DFG) Grants No. YE 232/2-2 and No. MC 9/22-1. S.K. acknowledges the support from the Philipp Schwartz Initiative of the Alexander von Humboldt Foundation.

DATA AVAILABILITY

The data that support the findings of this article are not publicly available upon publication because it is not technically feasible and/or the cost of preparing, depositing, and hosting the data would be prohibitive within the terms of this research project. The data are available from the authors upon reasonable request.

APPENDIX A: EQUILIBRIUM MAGNETIZATION TEXTURE

To identify possible equilibrium magnetization textures in DMI-free nanotubes, we introduce the following parametrization of the unit magnetization, $\boldsymbol{m} = \boldsymbol{e}_1 \cos\varphi \sin\vartheta + \boldsymbol{e}_2 \cos\vartheta + \boldsymbol{e}_3 \sin\varphi \sin\vartheta$, where $\{\vartheta, \varphi\} = \{\vartheta(\xi_1), \varphi(\xi_2)\}$. The equilibrium values of ϑ and φ are determined by the equations $\delta\mathcal{E}/\delta\vartheta = 0$ and $\delta\mathcal{E}/\delta\varphi = 0$. By solving these equations we find homogeneous and periodic equilibrium states.

The first is the vortex state. This state corresponds to the flux-free magnetization distribution, in which magnetization is oriented tangentially to the cylindrical surface, with $\boldsymbol{m} = \pm\boldsymbol{e}_1$, i.e., $\vartheta = \pi/2$ and $\cos\varphi = \pm 1$. The energy of the vortex state is $\mathcal{E}^{\mathrm{v}} = \varkappa^2$.

Another possible equilibrium configuration is the periodic magnetization distribution with $\vartheta = \pi/2$ and φ defined by a pendulum equation,

$$\partial_{11}\varphi - \lambda \sin\varphi \cos\varphi = 0, \quad \lambda = 1 + \varepsilon, \tag{A1}$$

with a solution,

$$\varphi = \mathrm{am}\left(\sqrt{\mathfrak{C}}\xi_1 \middle| -\frac{\lambda}{\mathfrak{C}}\right). \tag{A2}$$

Here, $\mathfrak{C}$ is an integration constant. The solution (A2) has a period

$$T = \frac{4}{\sqrt{\mathfrak{C}}}\mathrm{K}\left(-\frac{\lambda}{\mathfrak{C}}\right) = \frac{2\pi}{q\varkappa}, \tag{A3}$$

which is entirely predefined by geometry. Here, q defines the $2q$ number of domain walls on the cylindrical surface. The energy of the periodic solution is defined as

$$\mathcal{E}^{\mathrm{p}} = \mathcal{E}^{\mathrm{v}} - \mathfrak{C} - 2q\varkappa\left[\varkappa - \frac{2\sqrt{\mathfrak{C}}}{\pi}\mathrm{E}\left(-\frac{\lambda}{\mathfrak{C}}\right)\right], \tag{A4}$$

where $\mathrm{E}(x)$ is the complete elliptic integral of the second kind [71]. For a planar film, the transition between the homogeneous and periodic state is characterized by an infinite increase in the period of the spiral state [65]. Although for the cylindrical surface the period is finite at the transition point, for the limit case $\mathfrak{C} \to 0$ one has $T \to \infty$. Using that $\mathfrak{C} \to 0$ in this limit, we obtain from the equality $\mathcal{E}^{\mathrm{p}} = \mathcal{E}^{\mathrm{v}}$ the analytical expression for the critical curvature value $\varkappa_c$:

$$\varkappa_c = \frac{2\sqrt{1+\varepsilon}}{\pi}. \tag{A5}$$

In the limit case of vanishing easy-surface anisotropy ($\varepsilon = 0$) the critical curvature is defined as $\varkappa_0 = 2/\pi$ that is the same as for nanotubes with easy-normal anisotropy [56] and analogous to the effect of spontaneous formation of the onion state

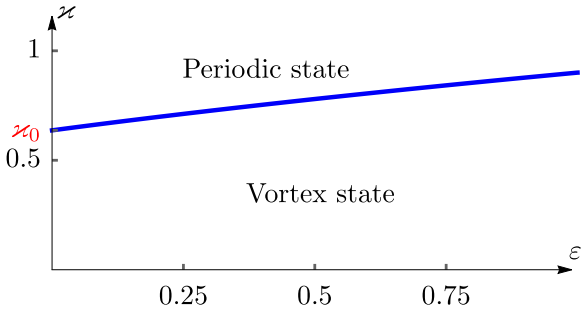

FIG. 6. Phase diagram of equilibrium magnetization textures in a DMI-free magnetic nanotube. The parameter space, curvature $\varkappa$ – easy-surface anisotropy ε, hosts two possible equilibrium configurations: periodic state and vortex state. The boundary curve is plotted using the prediction (A5).

in nanorings when curvature exceeds some critical value [72]. The phase diagram of equilibrium states is shown in Fig. 6.

APPENDIX B: MAGNETIC NANOTUBE WITH BULK-TYPE DMI

1. Micromagnetic energy in a ψ-frame

For the case of bulk-type DMI, one can obtain from the energy (1) a term that is quadratic with respect to the magnetization components, i.e., so-called effective anisotropy in the form $\mathscr{E}_{\mathrm{A}}^{b(\mathrm{eff})} = \mathcal{K}_{\alpha\beta} m_\alpha m_\beta$, where $\mathcal{K}_{\alpha\beta}$ is the effective total anisotropy matrix with coefficients

$$\mathcal{K}_{\alpha\beta} = \begin{pmatrix} \varkappa^2 - 1 & d\varkappa/2 & 0 \\ d\varkappa/2 & 0 & 0 \\ 0 & 0 & \varepsilon + \varkappa^2 \end{pmatrix}. \tag{B1}$$

This matrix has nondiagonal components. This means that the homogeneous magnetization structure is not oriented along the curvilinear basis, i.e., magnetization deviates from $\boldsymbol{e}_1$ direction by an angle $\psi \approx -d\varkappa/2$ (direction is defined by the sign of DMI constant d). One can easily diagonalize $\mathcal{K}_{\alpha\beta}$, by using a unitary transformation (rotation in a local tangential plane) of the vector $\boldsymbol{m}$

$$\begin{gathered} \boldsymbol{m} = U\boldsymbol{\mu}, \quad \boldsymbol{\mu} = U^{-1}\boldsymbol{m}, \quad \boldsymbol{\mu} = (\mu_1, \mu_2, \mu_3)^{\mathrm{T}}, \\ U = \begin{pmatrix} \cos\psi & -\sin\psi & 0 \\ \sin\psi & \cos\psi & 0 \\ 0 & 0 & 1 \end{pmatrix}. \end{gathered} \tag{B2}$$

By choosing $\psi = \arctan[(1 - \varkappa^2 - \mathcal{K}_1^b)/(d\varkappa)]$ as the rotation angle, where $\mathcal{K}_1^b = \sqrt{(1-\varkappa^2)^2 + d^2\varkappa^2}$, it is possible to reduce the anisotropy energy (B1) to the form

$$\begin{gathered} \mathscr{E}_{\mathrm{A}}^{b(\mathrm{eff})} = -\mathcal{K}_1^b \mu_1^2 + \mathcal{K}_3^b \mu_3^2, \quad \mathcal{K}_1^b \approx 1 - \varkappa^2\left(1 - \frac{d^2}{2}\right), \\ \mathcal{K}_3^b = \varepsilon + \frac{1 + \varkappa^2 - \mathcal{K}_1^b}{2} \approx \varepsilon + \varkappa^2\left(1 - \frac{d^2}{4}\right). \end{gathered}$$

Here, coefficient $\mathcal{K}_1^b$ characterizes the strength of the effective easy-axis anisotropy, while $\mathcal{K}_3^b$ gives the strength of the effective easy-surface anisotropy. The direction of the effective easy axis is determined by $\boldsymbol{e}_1^\psi$ and the hard axis by $\boldsymbol{e}_3^\psi$,

$$\begin{aligned} \boldsymbol{e}_1^\psi &= \boldsymbol{e}_1 \cos\psi + \boldsymbol{e}_2 \sin\psi, \\ \boldsymbol{e}_2^\psi &= -\boldsymbol{e}_1 \sin\psi + \boldsymbol{e}_2 \cos\psi, \\ \boldsymbol{e}_3^\psi &= \boldsymbol{n} = \boldsymbol{e}_3. \end{aligned} \tag{B3}$$

Note that for any finite ψ, the effective anisotropy direction $\boldsymbol{e}_1^\psi$ deviates from the magnetic anisotropy direction $\boldsymbol{e}_1$. This deviation vanishes in tubes with zero DMI ($d \to 0$).

Apart from the effective anisotropy, curvature shows up in the effective DMI. In the new frame of reference (rotated ψ-frame), the mesoscale DMI energy reads

$$\begin{aligned} \mathscr{E}_{\mathrm{D}}^{b(\mathrm{eff})} &= \mathcal{D}_{\beta 3}^{b(\alpha)}(\mu_\beta \partial_\alpha \mu_3 - \mu_3 \partial_\alpha \mu_\beta), \\ \mathcal{D}_{13}^{b(1)} &= -2\varkappa\cos\psi - d\sin\psi \approx -2\varkappa + \frac{d^2}{2}\varkappa, \\ \mathcal{D}_{23}^{b(1)} &= -d\cos\psi + 2\varkappa\sin\psi \approx -d - d\varkappa^2, \\ \mathcal{D}_{13}^{b(2)} &= d\cos\psi \approx d, \quad \mathcal{D}_{23}^{b(2)} = -d\sin\psi \approx \frac{d^2}{2}\varkappa. \end{aligned} \tag{B4}$$

With this, we get to the energy density in the form of (3).

2. Static DW solution

We consider the no-driving case $h = 0$, in which case the ground state is defined by the set of static equations $\delta\mathcal{E}^b/\delta\theta = 0$ and $\delta\mathcal{E}^b/\delta\phi = 0$, which read

$$\begin{aligned} &\partial_{11}\theta + \partial_{22}\theta + \cos\phi\sin^2\theta\left[\mathcal{D}_{13}^{b(1)}\partial_1\phi + \mathcal{D}_{13}^{b(2)}\partial_2\phi\right] \\ &\quad - \sin\theta\cos\theta\left[(\partial_1\phi)^2 + (\partial_2\phi)^2\mathcal{K}_1^b + \mathcal{K}_3^b\sin^2\phi\right. \\ &\quad \left. + \mathcal{D}_{23}^{b(1)}\partial_1\phi + \mathcal{D}_{23}^{b(2)}\partial_2\phi\right] = 0, \\ &\partial_1(\sin^2\theta\,\partial_1\phi) + \partial_2(\sin^2\theta\,\partial_2\phi) \\ &\quad + \sin\theta\cos\theta\left[\mathcal{D}_{23}^{b(1)}\partial_1\theta + \mathcal{D}_{23}^{b(2)}\partial_2\theta\right] \\ &\quad - \cos\phi\sin^2\theta\left[\mathcal{K}_3^b\sin\phi + \mathcal{D}_{13}^{b(1)}\partial_1\theta + \mathcal{D}_{13}^{b(2)}\partial_2\theta\right] = 0. \end{aligned} \tag{B5}$$

Without DMI ($d = 0$), the vortex ground state of the system with energy (1) is doubly degenerated: $\theta = 0$ and $\theta = \pi$. The transition between domains of different ground states forms a DW. Structure of the DW can be found as a solution of (B5) with boundary conditions $\cos\theta(\pm\infty) = \mp p$. This solution is well known,

$$\theta_{\mathrm{DW}}^0(\xi_2) = 2\arctan e^{p\xi_2/\Delta}, \quad \cos\phi_{\mathrm{DW}}^0 = \pm 1, \tag{B6}$$

where $\Delta = 1/\sqrt{\mathcal{K}_1^b} = 1/\sqrt{1-\varkappa^2}$ is the width of a static DW. Nevertheless, the DW solution (B6) does not satisfy Eq. (B5) in case $d \neq 0$. In the following, we introduce the deformation of the DW solution (B6) induced by the DMI, considering DMI as a small perturbation. For this purpose, we introduce small deviations from the nonperturbed solution (B6)

$$\theta = \theta_{\mathrm{DW}}^0 + \vartheta, \quad \phi = \phi_{\mathrm{DW}}^0 + \frac{\varphi}{\sin\theta_{\mathrm{DW}}^0(\xi_2)}. \tag{B7}$$

Substituting now (B7) into (B5) and linearizing the obtained equation with respect to the deviations ϑ and φ, the following equations for the deviations ϑ and φ,

$$\vartheta'' + \left(\frac{2}{\cosh^2\zeta} - 1\right)\vartheta = 0, \tag{B8a}$$

$$\varphi'' + \left(\frac{2}{\cosh^2\zeta} - \alpha^2\right)\varphi = \frac{\beta^b}{\cosh^2\zeta}, \tag{B8b}$$

where $\zeta = \xi_2/\Delta$ and $\partial_1\vartheta = \partial_{11}\vartheta = \partial_1\varphi = \partial_{11}\varphi = 0$, $\alpha = \sqrt{1 + \mathcal{K}_3^b/\mathcal{K}_1^b}$, and $\beta^b = p\,\mathcal{C}\mathcal{D}_{13}^{b(2)}/\sqrt{\mathcal{K}_1^b}$. In (B8) prime denotes the derivative with respect to ζ.

The nontrivial solution of the homogeneous Eq. (B8a) $\vartheta = \mathrm{d}\theta_{\mathrm{DW}}^0/\mathrm{d}\zeta = 1/\cosh\zeta$ corresponds to the Goldstone mode of the DW (B6). The function $\varphi(\zeta)$ is exponentially localized, $\varphi \propto \beta^b \exp(-\alpha\zeta)$ when $\zeta \to \infty$, and tends to $\beta^b/(2-\alpha^2)$ when $\zeta \to 0$.

3. Magnetostatic energy

The most contribution to the magnetostatic energy is generated by the interaction of surface charges, induced by the magnetization component normal to the tube's surface, $\sigma^{\pm} = \boldsymbol{m}\cdot\boldsymbol{n}^{\pm} = \pm\mu_3$ at surfaces $R^{\pm} = R \pm W/2$. The corresponding energy term $\mathcal{E}_{\mathrm{MS}}^{\sigma-\sigma}$ is local in the thin-shell limit, scaling as shell thickness W. We can calculate this contribution as

$$E_{\mathrm{MS}}^{\sigma-\sigma} = \frac{\mu_0 M_{\mathrm{s}}}{2}\int(\sigma^{+}U_{\sigma}^{+} + \sigma^{-}U_{\sigma}^{-})\mathrm{d}x_1\mathrm{d}x_2, \tag{B9}$$

where $U_{\sigma}^{\pm} = U_{\sigma}(x_3 = R^{\pm})$ is the potential of the surface charges given by

$$U_{\sigma}(\mathbf{x}) = \frac{M_{\mathrm{s}}}{4\pi}\iint_{x_3'=R^{\pm}}\frac{\sigma(\mathbf{x}')}{|\mathbf{x}-\mathbf{x}'|}\mathrm{d}x_1'\mathrm{d}x_2'.$$

Following the approach in [22], we expand the cylindrical Green's function in terms of Bessel functions $J_N(x)$ and perform the integral over x_1', obtaining

$$U_{\sigma}(x_2,x_3) = \frac{M_{\mathrm{s}}}{2}\int_0^{\infty}\mathrm{d}k\,J_0(kx_3)[R^{+}J_0(kR^{+}) - R^{-}J_0(kR^{-})]\int_{-\infty}^{\infty}\mathrm{d}x_2' e^{-k|x_2-x_2'|}\mu_3^{+}(x_2').$$

Next, using the integral representation $e^{-k|x_2-x_2'|} = \frac{1}{2\pi}\int_{-\infty}^{\infty}\frac{2k}{k^2+q^2}e^{iq(x_2-x_2')}\mathrm{d}q$, substituting the resulting potential to (B9), and integrating over x_1, we arrive at

$$E_{\mathrm{MS}}^{\sigma-\sigma} = \frac{1}{2}\mu_0 M_{\mathrm{s}}^2\int_{-\infty}^{\infty}\mathrm{d}q \times\int_0^{\infty}\frac{k\mathrm{d}k}{k^2+q^2}[R^{+}J_0(kR^{+}) - R^{-}J_0(kR^{-})]^2 \times\int_{-\infty}^{\infty}\mathrm{d}x_2 e^{iqx_2}\mu_3^{+}(x_2)\int_{-\infty}^{\infty}\mathrm{d}x_2' e^{-iqx_2'}\mu_3^{+}(x_2').$$

After having integrated over k and expanded the result in powers of W (thin-shell limit), we see that

$$E_{\mathrm{MS}}^{\sigma-\sigma} \simeq \frac{1}{2}\mu_0 M_{\mathrm{s}}^2 RW\int_{-\infty}^{\infty}\widetilde{\mu}_3^{+}(-q)\widetilde{\mu}_3^{+}(q)\mathrm{d}q, \tag{B10}$$

where $\widetilde{\mu}_3^{+}(q)$ is a Fourier transform of $\mu_3^{+}(x)$. Applying Parseval's theorem, we get

$$E_{\mathrm{MS}}^{\sigma-\sigma} \simeq \frac{1}{2}\mu_0 M_{\mathrm{s}}^2(2\pi R)W\int_{-\infty}^{\infty}dx_2|\mu_3(x_2)|^2, \tag{B11}$$

which allows us to directly include this term to the energy density (3) as $\mathcal{E}_{\mathrm{MS}}^{\sigma-\sigma} = wQE_{\mathrm{MS}}^{\sigma-\sigma}/E_0 = w\iint\mu_3^2\mathrm{d}\xi_1\mathrm{d}\xi_2$ by shifting the anisotropy ratio as $\varepsilon = \epsilon + Q^{-1}$, which emerges then in the effective anisotropy constant $\mathcal{K}_3^b$ (4).

Using ansatz (5) for the case of bulk-type DMI, we substitute $\mu_3 = \sin\Phi/\cosh(\xi_2/\Delta)$ and obtain $\mathcal{E}_{\mathrm{MS}}^{\sigma-\sigma} = w(2\pi/\varkappa)2\Delta\sin^2\Phi$, as appears in (6) derived from (1).

The volume and geometric magnetostatic charges for the magnetization distribution given by (5) are as follows:

$$\rho^b = \frac{1}{\Delta}\frac{\tanh(\xi_2/\Delta)}{\cosh(\xi_2/\Delta)}\cos\Phi; \quad g^b = -\frac{1}{\xi_3}\frac{\sin\Phi}{\cosh(\xi_2/\Delta)}.$$

The magnetic symmetry of terms corresponding to interactions $\mathcal{E}_{\mathrm{MS}}^{\rho-\rho}$, $\mathcal{E}_{\mathrm{MS}}^{g-g}$, and $\mathcal{E}_{\mathrm{MS}}^{\sigma-g}$ restricts symmetry breaking and cannot lead to chiral effects [43], resulting just in a correction of order $\sim o(w)$ [39,40,62,64] to the total energy. The remaining terms $\mathcal{E}_{\mathrm{MS}}^{\sigma-\rho}$ and $\mathcal{E}_{\mathrm{MS}}^{g-\rho}$, while generally allowing for nonlocal chiral effects, in our case, conserve the chiral symmetry because of the same parity of the components μ_2 and μ_3 with respect to $\xi_2 \to -\xi_2$.

We conclude that for the case of a DW in a nanotube with bulk-type DMI only local chiral effects are present. The account of the local magnetostatic contribution (B11) is sufficient for the considered range of geometrical and material parameters.

4. Exact form of the equations of motion for DW

The equations of motion can be derived from the Lagrangian $\mathcal{L}$ and the dissipative function $\mathcal{R}$,

$$\mathcal{L} = -\iint\phi\dot{\theta}\sin\theta\mathrm{d}\xi_1\mathrm{d}\xi_2 - \mathcal{E}, \tag{B12}$$

$$\mathcal{R} = \frac{\eta}{2}\iint(\dot{\theta}^2 + \dot{\phi}^2\sin^2\theta)\mathrm{d}\xi_1\mathrm{d}\xi_2, \tag{B13}$$

where η is the Gilbert damping parameter.

By substituting the ansatz (8) into (B13) one obtains

$$\frac{\mathcal{L}_{\mathrm{DW}}^b}{2\pi/\varkappa} = 2p\Phi\dot{q} - \frac{\mathcal{E}_{\mathrm{DW}}^b}{2\pi/\varkappa},$$
$$\frac{\mathcal{R}_{\mathrm{DW}}^b}{2\pi/\varkappa} = \frac{\eta}{\Delta}[\dot{q}^2 + \dot{\Phi}^2\Delta^2 + c\dot{\Delta}^2], \tag{B14}$$

with total energy in an external magnetic field

$$\frac{\mathcal{E}_{\mathrm{DW}}^b}{2\pi/\varkappa} = \frac{2}{\Delta} + 2\Delta\left(\mathcal{K}_1^b + \mathcal{K}_3^b\sin^2\Phi\right) + p\,\pi\mathcal{D}_{13}^{b(2)}\sin\Phi + \frac{\mathcal{E}_{\mathrm{Z}}^b}{2\pi/\varkappa},$$
$$\frac{\mathcal{E}_{\mathrm{Z}}^b}{2\pi/\varkappa} = -4h\begin{cases} p\,q\cos\psi - \frac{\pi}{2}\Delta\cos\Phi\sin\psi, & \boldsymbol{h}||\boldsymbol{e}_1 - \text{vortex magnetic field},\\ p\,q\sin\psi + \frac{\pi}{2}\Delta\cos\Phi\cos\psi, & \boldsymbol{h}||\boldsymbol{e}_2 - \text{axial magnetic field}.\end{cases} \tag{B15}$$

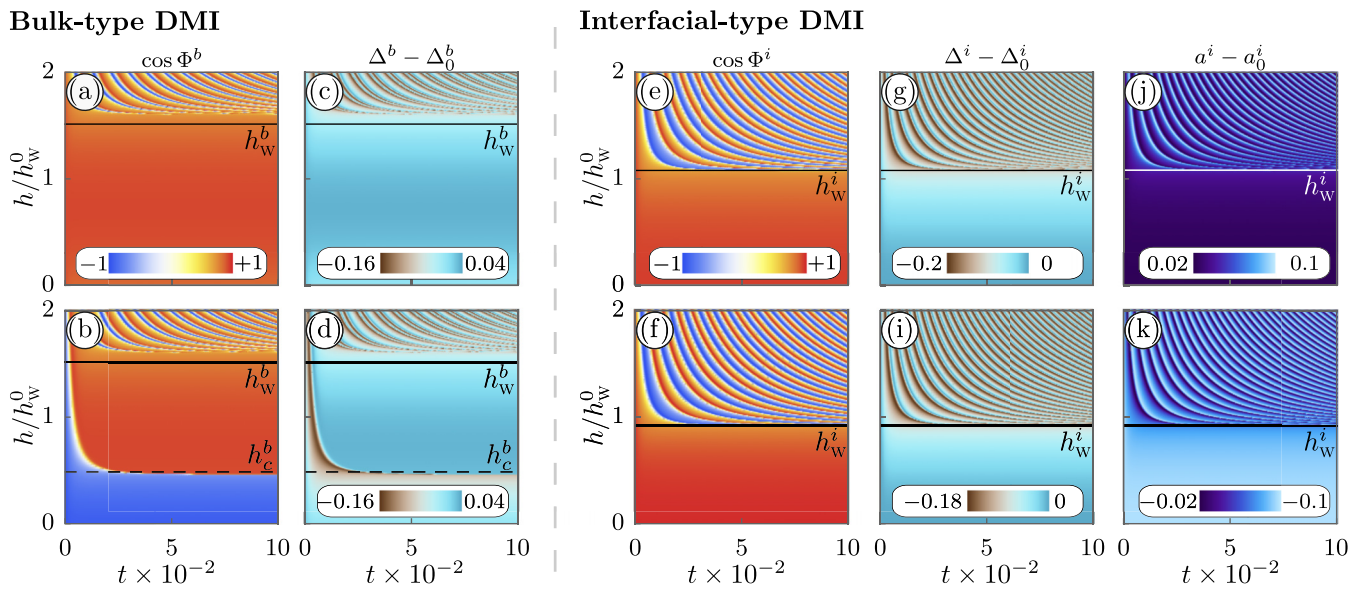

FIG. 7. Typical evolution of the DW phase, width, and phase slope in nanotubes with bulk- and interfacial-type DMI in terms of density plot. Panels (a)–(d) correspond to the case of bulk-type DMI: Top row shows the evolution of DW phase (a) and width (c) for the "favorable" DW helicity, bottom row shows the evolution of DW phase (b) and width (d) for the "unfavorable" DW helicity. Panels are plotted by means of a numerical solution of set (B16) for the case of a vortex magnetic field. The horizontal-solid and dashed lines correspond to the values of the Walker and chiral fields, respectively, defined in (12). Panels (e)–(k) correspond to the case of interfacial-type DMI: Top row shows the evolution of DW phase (e), width (g), and phase slope (j) for the positive DMI strength ($d > 0$), bottom row shows the evolution of DW phase (f), width (i), and phase slope (k) for the negative DMI strength ($d < 0$). Panels are plotted via a numerical solution of set (C10). The horizontal-solid line corresponds to the value of the Walker fields (25). In all cases we use $p = +1$, $\varepsilon = 0.5$, $|d| = 0.25$, $\varkappa = 0.2$, and $\eta = 0.1$.

Lagrangian and dissipative function (B14) produce the following set of equations of motion:

$$\frac{\eta}{\Delta}\dot{q} + p\dot{\Phi} = -\frac{\varkappa}{4\pi}\frac{\partial \mathcal{E}^b_{\rm Z}}{\partial q},$$
$$p\dot{q} - \eta\Delta\dot{\Phi} = 2p\frac{\mathcal{D}^{b(2)}_{13}}{d_0}\cos\Phi + \mathcal{K}^b_3\Delta\sin 2\Phi + \frac{\varkappa}{4\pi}\frac{\partial \mathcal{E}^b_{\rm Z}}{\partial \Phi},$$
$$c\eta\frac{\dot{\Delta}}{\Delta} = \frac{1}{\Delta^2} - \mathcal{K}^b_1 - \mathcal{K}^b_3\sin^2\Phi - \frac{\varkappa}{4\pi}\frac{\partial \mathcal{E}^b_{\rm Z}}{\partial \Delta}. \qquad \text{(B16)}$$

(i) For the case of a vortex magnetic field ($\boldsymbol{h}\|\boldsymbol{e}_1$), the third equation in (B16) shows that Δ relaxes towards its equilibrium value $\Delta^b_0 \approx 1/\sqrt{\mathcal{K}^b_1 + \mathcal{K}^b_3\sin^2\Phi^b}$. The characteristic time of this relaxation is proportional to the damping $\propto \eta$ [67]. Usually $\eta \ll 1$; therefore, one can conclude that the DW width is a slave variable $\Delta[\Phi(t)]$, and DW dynamics can be described by the set (10) with the equilibrium DW width $\Delta = \Delta^b_0$. The typical evolution of DW parameters (width Δ^b and phase Φ^b) for the case of bulk-type DMI is plotted in Figs. 7(a)–7(d) with the corresponding chiral and Walker fields. The dependencies of these critical fields as functions of curvature and torsion are presented in Figs. 8(a) and 8(b). Note that for the given parameters ($p\mathcal{C} = +1$), the change of the sign of the DMI strength d results in the switching between "favorable" and "unfavorable" DWs.

(ii) For the axial magnetic field ($\boldsymbol{h}\|\boldsymbol{e}_2$), the third equation in (B16) shows that Δ relaxes to the value $\Delta^b_0 = 1/\sqrt{\mathcal{K}^b_1 + \mathcal{K}^b_3\sin^2\Phi^b - \pi h\cos\psi}$, i.e., external field results in a small deformation of DW shape. As mentioned in the Sec. III B 2, here we consider fields smaller than the Walker field, $h \ll h^0_{\rm w}$. In this case, field-induced deformations are negligible, and the equilibrium DW width can be defined as $\Delta^b_0 \approx 1/\sqrt{\mathcal{K}^b_1 + \mathcal{K}^b_3\sin^2\Phi^b}$. Thus, we conclude that here the DW width is also a slave variable $\Delta[\Phi(t)]$, and the DW dynamics can be described by the set (14) with the equilibrium DW width $\Delta = \Delta^b_0$.

APPENDIX C: MAGNETIC NANOTUBE WITH INTERFACIAL-TYPE DMI

1. Static DW solution

In the no-driving case $h = 0$, the ground state is defined by the set of static equations $\delta\mathcal{E}^i/\delta\Theta = 0$ and $\delta\mathcal{E}^i/\delta\Phi = 0$, which read

$$-2(\partial_{11}\Theta + \partial_{22}\Theta) + \sin 2\Theta\big[(\partial_1\Phi)^2 + (\partial_2\Phi)^2 + \mathcal{K}^i_1 + \mathcal{K}^i_3\sin^2\Phi\big] - 2\mathcal{D}^{i(1)}_{13}\cos\Phi\sin^2\Theta\partial_1\Phi + \mathcal{D}^{i(2)}_{23}\sin 2\Theta\partial_2\Phi = 0,$$
$$-2[\partial_1(\sin^2\Theta\partial_1\Phi) + \partial_2(\sin^2\Theta\partial_2\Phi)] + \mathcal{K}^i_3\sin 2\Phi\sin^2\Theta + 2\mathcal{D}^{i(1)}_{13}\cos\Phi\sin^2\Theta\partial_1\Theta - \mathcal{D}^{i(2)}_{23}\sin 2\Theta\partial_2\Theta = 0. \qquad \text{(C1)}$$

Similarly to Appendix B 2, for the case of a DMI-free nanotube the ground state of the system is doubly degenerated: $\Theta = 0$ and $\Theta = \pi$. The DW structure is defined by (B6)

$$\Theta^0_{\rm DW}(\xi_2) = 2\arctan e^{p\xi_2/\Delta}, \quad \cos\Phi^0_{\rm DW} = \pm 1, \qquad \text{(C2)}$$

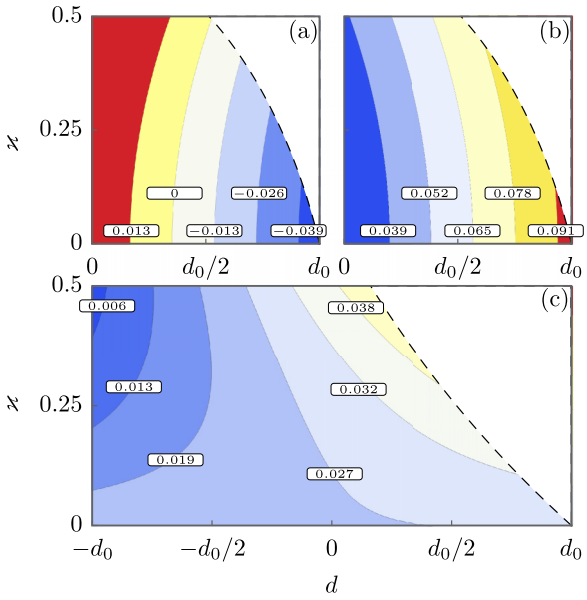

FIG. 8. Critical fields as functions of curvature and DMI strength. Panels (a) and (b) show the dependencies of chiral h_c^b and Walker h_w^b fields, respectively, for bulk-type DMI. Field values are shown as contour labels and given in units of anisotropy field H_A. Panel (c) shows the Walker field h_w^i for the interfacial-type DMI. Black dashed lines correspond to the critical DMI, which separates uniform and periodical (white area) magnetization distributions [56]. In all cases we use $p = +1$, $\mathcal{C} = +1$, $\varepsilon = 0.5$, and $\eta = 0.1$.

The DW solution (B6) does not satisfy Eq. (C1) in the case $d \neq 0$. Here, we will also introduce small deviations (B7) from the nonperturbed solution. Substituting (B7) into (C1) and linearizing the resulting equation with respect to the deviations, we obtain the following equations for the deviations ϑ and φ,

$$\vartheta'' + \left(\frac{2}{\cosh^2\zeta} - 1\right)\vartheta = 0, \tag{C3a}$$

$$\varphi'' + \left(\frac{2}{\cosh^2\zeta} - \alpha^2\right)\varphi = \beta^i \frac{\tanh\zeta}{\cosh\zeta}, \tag{C3b}$$

where $\beta^i = p\mathcal{D}_{23}^{i(2)}/\sqrt{\mathcal{K}_1^b}$. Equation (C3a) coincides with Eq. (B8a), while the function $\varphi(\zeta)$ is also exponentially localized, $\varphi \propto \beta^i \exp(-\alpha\zeta)$ when $\zeta \to \infty$ but has a linear behavior $\varphi \propto \beta^i\zeta/(2-\alpha^2)$ when $\zeta \to 0$.

The set of equations (C3) was previously obtained for DWs in straight biaxial wires with bulk-type DMI [12].

2. Magnetostatic energy

For the case of a DW in a nanotube with interfacial DMI given by ansatz (19), the surface-charge-induced magnetostatic energy term (B11), takes the form

$$E_{\mathrm{MS}}^{\sigma-\sigma} \simeq \frac{1}{2}\mu_0 M_s^2 2\pi RW\Delta\left(1 - \pi a\frac{\cos 2\Phi}{\sinh(\pi a)}\right), \tag{C4}$$

which can be accounted for by the renormalization of the anisotropy constant $\mathcal{K}_3^i$ in (18) through shifting the anisotropy ratio as $\varepsilon = \epsilon + Q^{-1}$.

The volume and geometric magnetostatic charges for the magnetization distribution given by (19) are

$$\rho^i = \frac{1}{\Delta}\frac{a\sin\left(\Phi_0 + a\frac{\xi_2}{\Delta}\right) + \tanh\frac{\xi_2}{\Delta}\cos\left(\Phi_0 + a\frac{\xi_2}{\Delta}\right)}{\cosh\frac{\xi_2}{\Delta}};$$

$$g^i = -\frac{1}{\xi_3}\frac{\sin\left(\Phi_0 + a\frac{\xi_2}{\Delta}\right)}{\cosh\frac{\xi_2}{\Delta}}. \tag{C5}$$

Note that in the case of interfacial-type DMI, the magnetization components m_2 and m_3 have different parity with respect to $\xi_2 \to -\xi_2$. This leads to the emergence of the DW configuration with a favorable phase slope a, as both contributions $E_{\mathrm{MS}}^{g-\rho}$ and $E_{\mathrm{MS}}^{\sigma-\rho}$ embrace the term $\propto a\cos\Phi_0^2$. However, the DW topological charge $p = \pm 1$ defining the component m_1 (19) plays no role in the magnetostatic energy of the studied system, which means chiral effects are absent. The preferable phase slope a is the same for any p and any DW helicity $\mathcal{C} = \cos\Phi_0 = \pm 1$.

In the local interactions framework, the preferable sign of phase slope a is predetermined by the intrinsic DMI constant d of the material, sign$a$ = sign$d$. However, the magnetostatic contribution prefers a particular sign of a independent of d. The resulting configuration depends on the interplay of geometrical and material parameters in a specific system, as we proceed to derive.

The total magnetostatic energy can be written as

$$E_{\mathrm{MS}} = \frac{1}{2}\mu_0 M_s\pi\int_0^\infty \left\{k^2 G_1^2(k)\Lambda_1 - kG_1(k)G_0(k)[\Lambda_2 - \widetilde{\Lambda}_1] - G_0^2(k)\widetilde{\Lambda}_2\right\}\mathrm{d}k, \tag{C6}$$

where we use the notations a là [22],

$$G_\nu(k) = \int_{R_1}^{R_2} J_\nu(kx_3)x_3\mathrm{d}x_3;$$

$$\Lambda_1 = \int_{-\infty}^{\infty}\mathrm{d}x_2\, m_3(x_2)\int_{-\infty}^{\infty}\mathrm{d}x_2' e^{-k|x_2-x_2'|}m_3(x_2');$$

$$\widetilde{\Lambda}_1 = \int_{-\infty}^{\infty}\mathrm{d}x_2\, m_3(x_2)\int_{-\infty}^{\infty}\mathrm{d}x_2' e^{-k|x_2-x_2'|}\partial_{x_2'}m_2(x_2');$$

$$\Lambda_2 = \int_{-\infty}^{\infty}\mathrm{d}x_2\, m_2(x_2)\partial_{x_2}\int_{-\infty}^{\infty}\mathrm{d}x_2' e^{-k|x_2-x_2'|}m_3(x_2');$$

$$\widetilde{\Lambda}_2 = \int_{-\infty}^{\infty}\mathrm{d}x_2\, m_2(x_2)\partial_{x_2}\int_{-\infty}^{\infty}\mathrm{d}x_2' e^{-k|x_2-x_2'|}\partial_{x_2'}m_2(x_2').$$

The energy contributions $E_{\mathrm{MS}}^{\sigma-\rho}$ and $E_{\mathrm{MS}}^{g-\rho}$ are captured by the terms containing $\widetilde{\Lambda}_1$ and Λ_2. Using (19), applying $e^{-k|x_2-x_2'|} = \frac{1}{2\pi}\int_{-\infty}^{\infty}\frac{2k}{k^2+q^2}e^{iq(x_2-x_2')}\mathrm{d}q$, and leaving only the terms linear in a, we get

$$E_{\mathrm{MS}}^{\sigma-\rho} + E_{\mathrm{MS}}^{g-\rho} \simeq -\frac{\mu_0 M_s}{4}a\pi^2 W^2\Delta. \tag{C7}$$

Therefore, for any DW helicity the configuration with $a > 0$ is preferred by magnetostatics. We see from (20) and (C7) that for $d > 0$ both DMI and magnetostatics favor the configuration with $a > 0$ [corresponds to Figs. 4(c) and 4(d)]. However, if $d < 0$ [Fig. 4(e)], the two effects compete. The effective DMI constant $d + \pi w\varkappa/8Q$ defines the resulting phase slope: $d < -\pi w\varkappa/8Q$ results in $a < 0$, while

$d > -\pi w\varkappa/8Q$ would still favor $a > 0$. Interestingly, the threshold DMI value depends on the film thickness w and curvature $\varkappa$, which enables tailoring the interplay between local and nonlocal effects on the DW profile at the nanotube production stage. In a nanotube with $d < 0$ and $W/R = -8Qd/\pi$ the DMI-induced effects can be virtually compensated, and the resulting DW structure will be described by (B6).

3. Exact form of the equations of motion for DW

By substituting the Ansatz (22) into (B13) one obtains

$$\frac{\mathcal{L}^i_{\rm DW}}{2\pi/\varkappa} = 2p[\Phi\dot q + ca\dot\Delta] - \frac{\mathcal{E}^i_{\rm DW}}{2\pi/\varkappa}, \quad \frac{\mathcal{R}^i_{\rm DW}}{2\pi/\varkappa} = \frac{\eta}{\Delta}[\dot q^2 + (\dot q a - \dot\Phi\Delta)^2 + c(\Delta\dot a - \dot\Delta a)^2 + c\dot\Delta^2], \tag{C8}$$

with total energy in an external magnetic field

$$\frac{\mathcal{E}^i_{\rm DW}}{2\pi/\varkappa} = \frac{2}{\Delta}(1+a^2) + 2a\mathcal{D}^{i(2)}_{23} - a\Delta\frac{\pi w\varkappa}{4Q} + \Delta\left[2\mathcal{K}^i_1 + \mathcal{K}^i_3\left(1 - \pi a\frac{\cos 2\Phi}{\sinh(\pi a)}\right)\right] - 4phq. \tag{C9}$$

Lagrangian and dissipative function (C8) produce the following set of equations of motion:

$$\begin{aligned}
&\eta(1+a^2)\frac{\dot q}{\Delta} + (p-\eta a)\dot\Phi = 2ph,\\
&(p+\eta a)\dot q - \eta\Delta\dot\Phi = \pi a\Delta\mathcal{K}^i_3\frac{\sin 2\Phi}{\sinh(\pi a)},\\
&c\eta(1+a^2)\frac{\dot\Delta}{\Delta} + c(p-\eta a)\dot a = \frac{1}{\Delta^2}(1+a^2) - \mathcal{K}^i_1 - \frac{\mathcal{K}^i_3}{2}\left[1 - \pi a\frac{\cos 2\Phi}{\sinh(\pi a)}\right] + a\frac{\pi w\varkappa}{8Q},\\
&c(p+\eta a)\frac{\dot\Delta}{\Delta} - c\eta\dot a = \frac{2}{\Delta}\left(\frac{a}{\Delta} + \frac{\mathcal{D}^{i(2)}_{23}}{2} - \frac{\pi w\varkappa\Delta}{16Q}\right) + \mathcal{K}^i_3\frac{\pi}{2}\frac{\cos 2\Phi}{\sinh(\pi a)}[\pi a\coth(\pi a) - 1].
\end{aligned} \tag{C10}$$

In linear approximation with respect to the slope a,

$$\begin{aligned}
&\eta\frac{\dot q}{\Delta} + p(1-a\eta)\dot\Phi = 2ph,\\
&p(1+a\eta)\dot q - \eta\Delta\dot\Phi = \mathcal{K}^i_3\Delta\sin 2\Phi,\\
&c\eta\frac{\dot\Delta}{\Delta} + cp\dot a = \frac{1}{\Delta^2} - \mathcal{K}^i_1 - \mathcal{K}^i_3\sin^2\Phi + a\frac{\pi w\varkappa}{8Q},\\
&(p+\eta a)\dot\Delta - \eta\dot a\Delta = \frac{1}{c}\left(\mathcal{D}^{i(2)}_{23} - \Delta\frac{\pi w\varkappa}{8Q} + \frac{2a}{\Delta}\right)\\
&\qquad + 2a\mathcal{K}^i_3\Delta\cos 2\Phi.
\end{aligned} \tag{C11}$$

The third and fourth equations in (C11) demonstrate that Δ and a relax towards their equilibrium values $\Delta^i_0 = 1/\sqrt{\mathcal{K}^i_1 + \mathcal{K}^i_3\sin^2\Phi^i}$ and $a^i_0 = -(\mathcal{D}^{i(2)}_{23} - \frac{\pi w\varkappa}{8Q}\Delta^i_0)/(2/\Delta^i_0 + 2c\mathcal{K}^i_3\Delta^i_0\cos 2\Phi^i)$. The characteristic time of this relaxation is proportional to the damping $\propto\eta$ [67]. We conclude that the DW width and phase slope are slave variables, $\Delta[\Phi(t)]$ and $a[\Phi(t)]$, and the DW dynamics can be described by (23) with the equilibrium values of $\Delta = \Delta^i_0$ and $a = a^i_0$. The typical evolution of DW parameters (width Δ^i, phase Φ^i, and phase slope a^i) for the case of interfacial-type DMI is plotted in Figs. 7(e)–7(k), with the corresponding Walker field. The dependence of this field as a function of DMI strength and curvature for interfacial-type DMI is illustrated in Fig. 8(c).

APPENDIX D: DETAIL OF NUMERICAL SIMULATIONS

In order to verify our analytical calculations, we perform a set of numerical simulations with (i) OOMMF code [73] with additional packages for bulk-type DMI [74,75] and a modified package for interfacial-type DMI, and (ii) in-house developed python-based code. The modified package for OOMMF is based on the module developed by S. Rohart *et al.* [65]. The modified package is within the Supplemental Material [68].

1. OOMMF simulations

With OOMMF we consider only static problems [76]. In simulations we consider tubes of total length 250 nm, inner radius 24 nm, and thickness 3 nm, with cell size $1\times1\times1$ nm^3. We use the following artificial material parameters: exchange constant $A = 25\times10^{-12}$ J/m, saturation magnetization $M_s = 5\times10^5$ A/m, easy-axial anisotropy constant $K_a = 10^6$ J/m^3, easy-surface anisotropy constant $K_s = 0.34\times10^6$ J/m^3, and DMI constant $D = 1.25\times10^{-3}$ J/m^2. The effective easy-surface anisotropy constant accounting for magnetostatics was set to $K^{\rm eff}_s = K_s + \mu_0 M_s^2/2 = 0.5\times10^6$ J/m^3.

As exemplary experimental setups one can consider FeGe [75] for the case of bulk-type DMI and Pt/Co/Ni trilayer system [30] for the interfacial-type DMI. We estimate the parameters of these two systems in nanotubes of radius $R = 50$ nm and thickness $W = 6$ nm. (i) For FeGe we get $\Delta^b_0\ell \approx 6$ nm, $h_0H_{\rm A} \approx 25$ mT, $h^b_cH_{\rm A} \approx 3$ mT, and $h^b_wH_{\rm A} \approx 47$ mT. (ii) For Pt/Co/Ni we get $\Delta^i_0\ell \approx 15$ nm, $a^i_0/\ell \approx 0.01$ nm^{-1}, $h_0H_{\rm A} \approx 45$ mT, $h^i_cH_{\rm A} \approx (47+2p)$ mT (here, $p = \pm1$ corresponds to DW topological charge).

The numerical experiment consists of two steps. First, we relax the DW structure in an overdamped regime ($\eta = 0.5$) with a certain topological charge $p = +1$, i.e., we start with two sharp domains that are oriented in opposite directions. Next, we extract the DW parameters: DW position, phase, width, and phase slope. The results of numerical simulations are presented in Figs. 1–5.

2. Spin-lattice simulations

We consider a cylindrical surface as a square lattice with lattice constant s. Each node is characterized by a magnetic moment $\boldsymbol{m}_{\boldsymbol{k}}(t)$ that is located at the position $\boldsymbol{r}_{\boldsymbol{k}}$. Here, $\boldsymbol{k} = (i, j)$ is a two-dimensional vector that defines the magnetic moment and its position on the lattice with size $N_1 \times N_2$ ($i \in [1, N_1]$ and $j \in [1, N_2]$). Magnetic moments are ferromagnetically coupled. We are interested in the case when the system is a closed cylindrical surface; hence, we impose the periodical boundary conditions $\boldsymbol{m}_{(N_1+1,j)} = \boldsymbol{m}_{(1,j)}$ and $\boldsymbol{r}_{(N_1+1,j)} = \boldsymbol{r}_{(1,j)}$. The dynamics of magnetic system is governed by discrete Landau–Lifshitz–Gilbert equations.

The dynamical problem is considered as a set of $3N_1N_2$ ordinary differential equations with respect to $3N_1N_2$ unknown functions $m^x_{\boldsymbol{k}}(t)$, $m^y_{\boldsymbol{k}}(t)$, $m^z_{\boldsymbol{k}}(t)$. For given initial conditions, the set of Landau–Lifshitz–Gilbert equations is integrated numerically using the Runge–Kutta method in Python. For details of the workflow of the in-house developed code, see Ref. [56].

In simulations, we consider cylinders with $N_1 = 200$ and $N_2 = 10000$, the magnetic length $\ell \approx 6.37s$ (this value of magnetic length results in dimensionless curvature $\varkappa = 0.2$), DMI constant $d = 0.25$ (for bulk and interfacial DMI types), and anisotropy ratio $\varepsilon = 0.5$.

The numerical experiment consists of two steps. First, we relax the DW structure in an over-damped regime ($\eta = 0.5$) to relax the DW of a certain charge p and helicity $\mathcal{C}$ on the cylindrical surface. In the second step, we stimulate the DW motion by applying the magnetic field h with natural damping coefficient $\eta = 0.01$. The averaged DW velocity is obtained as $V = \frac{1}{T}\int_0^T \dot{q}\mathrm{d}t$, where $\dot{q}$ is extracted from the simulation data.

3. Movies of the domain wall motion

For better visualization of the field-induced motion of magnetic DWs in a nanotube with bulk-type DMI, we have prepared movies (see the Supplemental Material [68]) illustrating the wall dynamics:

(i) `video1_favorable_DW.mp4` shows the dynamics of a DW with topological charge $p = +1$ and initial helicity $\mathcal{C} = +1$;

(ii) `video2_unfavorable_DW.mp4` shows the dynamics of a DW with topological charge $p = +1$ and initial helicity $\mathcal{C} = -1$.

The data in these movies correspond to results obtained via numerical simulations. In all simulations, we used $d = 0.25$, $\varkappa = 0.25$, $h = 0.7h^0_{\mathrm{w}}$, and $\eta = 0.01$.

In both videos, the bottom-right panel displays a magnified view of the nanotube near the DW center, located between two green circles. The top-left panel presents an unrolled perspective of this zoomed-in region where the color scheme corresponds to magnetization component μ_2, and streamlines show the in-surface magnetization.

[1] D. A. Allwood, G. Xiong, M. D. Cooke, C. C. Faulkner, D. Atkinson, N. Vernier, and R. P. Cowburn, Submicrometer ferromagnetic NOT gate and shift register, Science **296**, 2003 (2002).

[2] D. A. Allwood, G. Xiong, C. C. Faulkner, D. Atkinson, D. Petit, and R. P. Cowburn, Magnetic domain–wall logic, Science **309**, 1688 (2005).

[3] S. S. P. Parkin, M. Hayashi, and L. Thomas, Magnetic domain-wall racetrack memory, Science **320**, 190 (2008).

[4] Z. Luo, A. Hrabec, T. P. Dao, G. Sala, S. Finizio, J. Feng, S. Mayr, J. Raabe, P. Gambardella, and L. J. Heyderman, Current-driven magnetic domain-wall logic, Nature (London) **579**, 214 (2020).

[5] J. Yang, C. Abert, D. Suess, and S.-K. Kim, Intrinsic DMI-free skyrmion formation and robust dynamic behaviors in magnetic hemispherical shells, Sci. Rep. **11**, 3886 (2021).

[6] G. Venkat, D. A. Allwood, and T. J. Hayward, Magnetic domain walls: Types, processes and applications, J. Phys. D **57**, 063001 (2024).

[7] A. Thiaville, S. Rohart, É. Jué, V. Cros, and A. Fert, Dynamics of Dzyaloshinskii domain walls in ultrathin magnetic films, Europhys. Lett. **100**, 57002 (2012).

[8] O. Boulle, S. Rohart, L. D. Buda-Prejbeanu, E. Jué, I. M. Miron, S. Pizzini, J. Vogel, G. Gaudin, and A. Thiaville, Domain wall tilting in the presence of the Dzyaloshinskii-Moriya interaction in out-of-plane magnetized magnetic nanotracks, Phys. Rev. Lett. **111**, 217203 (2013).

[9] S. Emori, U. Bauer, S.-M. Ahn, E. Martinez, and G. S. D. Beach, Current-driven dynamics of chiral ferromagnetic domain walls, Nat. Mater. **12**, 611 (2013).

[10] K.-S. Ryu, L. Thomas, S.-H. Yang, and S. Parkin, Chiral spin torque at magnetic domain walls, Nat. Nanotechnol. **8**, 527 (2013).

[11] A. Brataas, Chiral domain walls move faster, Nat. Nanotechnol. **8**, 485 (2013).

[12] V. P. Kravchuk, Influence of Dzialoshinskii-Moriya interaction on static and dynamic properties of a transverse domain wall, J. Magn. Magn. Mater. **367**, 9 (2014).

[13] K. V. Yershov, V. P. Kravchuk, D. D. Sheka, J. van den Brink, and A. Saxena, Domain wall diode based on functionally graded Dzyaloshinskii–Moriya interaction, Appl. Phys. Lett. **116**, 222406 (2020).

[14] O. V. Pylypovskyi, V. P. Kravchuk, O. M. Volkov, J. Fassbender, D. Sheka, and D. Makarov, Unidirectional tilt of domain walls in equilibrium in biaxial stripes with Dzyaloshinskii-Moriya interaction, J. Phys. D **53**, 395003 (2020).

[15] A. Thiaville, Y. Nakatani, J. Miltat, and Y. Suzuki, Micromagnetic understanding of current-driven domain wall motion in patterned nanowires, Europhys. Lett. **69**, 990 (2005).

[16] M. Yan, A. Kákay, S. Gliga, and R. Hertel, Beating the Walker limit with massless domain walls in cylindrical nanowires, Phys. Rev. Lett. **104**, 057201 (2010).

[17] K. V. Yershov, V. P. Kravchuk, D. D. Sheka, and Y. Gaididei, Curvature-induced domain wall pinning, Phys. Rev. B **92**, 104412 (2015).

[18] K. V. Yershov, V. P. Kravchuk, D. D. Sheka, and Y. Gaididei, Curvature and torsion effects in spin-current driven domain wall motion, Phys. Rev. B **93**, 094418 (2016).

[19] O. V. Pylypovskyi, D. D. Sheka, V. P. Kravchuk, K. V. Yershov, D. Makarov, and Y. Gaididei, Rashba torque driven domain wall motion in magnetic helices, Sci. Rep. **6**, 23316 (2016).

[20] J. A. Fernandez-Roldan and O. Chubykalo-Fesenko, Dynamics of chiral domain walls under applied current in cylindrical magnetic nanowires, APL Mater. **10**, 111101 (2022).

[21] M. Yan, C. Andreas, A. Kákay, F. García-Sánchez, and R. Hertel, Fast domain wall dynamics in magnetic nanotubes: Suppression of Walker breakdown and Cherenkov-like spin wave emission, Appl. Phys. Lett. **99**, 122505 (2011).

[22] P. Landeros and A. S. Núñez, Domain wall motion on magnetic nanotubes, J. Appl. Phys. **108**, 033917 (2010).

[23] M. Yan, C. Andreas, A. Kákay, F. Garcia-Sanchez, and R. Hertel, Chiral symmetry breaking and pair-creation mediated Walker breakdown in magnetic nanotubes, Appl. Phys. Lett. **100**, 252401 (2012).

[24] J. Otálora, J. López-López, P. Vargas, and P. Landeros, Chirality switching and propagation control of a vortex domain wall in ferromagnetic nanotubes, Appl. Phys. Lett. **100**, 072407 (2012).

[25] J. Otálora, J. López-López, A. Núñez, and P. Landeros, Domain wall manipulation in magnetic nanotubes induced by electric current pulses, J. Phys.: Condens. Matter **24**, 436007 (2012).

[26] J. Otálora, J. López-López, P. Landeros, P. Vargas, and A. Núñes, Breaking of chiral symmetry in vortex domain wall propagation in ferromagnetic nanotubes, J. Magn. Magn. Mater. **341**, 86 (2013).

[27] A. Goussev, J. M. Robbins, V. Slastikov, and O. A. Tretiakov, Dzyaloshinskii-Moriya domain walls in magnetic nanotubes, Phys. Rev. B **93**, 054418 (2016).

[28] M. C. Depassier, Speed of domain walls in thin nanotubes: The transition from the linear to the magnonic regime, Phys. Rev. B **100**, 144402 (2019).

[29] D. Mancilla-Almonacid, R. Jaeschke-Ubiergo, A. S. Núñez, and S. Allende, Ultrafast domain wall propagation due to the interfacial Dzyaloshinskii–Moriya interaction, Nanotechnology **31**, 125707 (2020).

[30] E. Josten, D. Raftrey, A. Hierro-Rodriguez, A. Sorrentino, L. Aballe, M. Lipińska-Chwałek, T. Jansen, K. Höflich, H. Kröncke, C. Dubourdieu *et al.*, Curvature-mediated spin textures in magnetic multi-layered nanotubes, arXiv:2103.13310.

[31] P. Landeros, J. A. Otálora, R. Streubel, and A. Kákay, Tubular geometries, in *Topics in Applied Physics* (Springer International Publishing, Cham, Switzerland, 2022), pp. 163–213.

[32] I. Dzyaloshinsky, A thermodynamic theory of "weak" ferromagnetism of antiferromagnetics, J. Phys. Chem. Solids **4**, 241 (1958).

[33] T. Moriya, Anisotropic superexchange interaction and weak ferromagnetism, Phys. Rev. **120**, 91 (1960).

[34] S. Woo, K. Litzius, B. Krüger, M.-Y. Im, L. Caretta, K. Richter, M. Mann, A. Krone, R. M. Reeve, M. Weigand *et al.*, Observation of room-temperature magnetic skyrmions and their current-driven dynamics in ultrathin metallic ferromagnets, Nat. Mater. **15**, 501 (2016).

[35] I. Lemesh, F. Büttner, and G. S. D. Beach, Accurate model of the stripe domain phase of perpendicularly magnetized multilayers, Phys. Rev. B **95**, 174423 (2017).

[36] F. Büttner, I. Lemesh, and G. S. D. Beach, Theory of isolated magnetic skyrmions: From fundamentals to room temperature applications, Sci. Rep. **8**, 4464 (2018).

[37] A. Bernand-Mantel, L. Camosi, A. Wartelle, N. Rougemaille, M. Darques, and L. Ranno, The skyrmion-bubble transition in a ferromagnetic thin film, SciPost Phys. **4**, 027 (2018).

[38] J. Schöpf, A. Thampi, P. Milde, D. Ivaneyko, S. Kondovych, D. Y. Kononenko, L. M. Eng, L. Jin, L. Yang, L. Wysocki *et al.*, Néel skyrmion bubbles in $La_{0.7}Sr_{0.3}Mn_{1-x}Ru_xO_3$ multilayers, Nano Lett. **23**, 3532 (2023).

[39] G. Carbou, Thin layers in micromagnetism, Math. Models Methods Appl. Sci. **11**, 1529 (2001).

[40] R. V. Kohn and V. V. Slastikov, Effective dynamics for ferromagnetic thin films: A rigorous justification, Proc. R. Soc. A **461**, 143 (2005).

[41] D. D. Sheka, V. P. Kravchuk, D. Peddis, G. Varvaro, M. Krupiński, M. Albrecht, D. Erb, S. Facsko, and D. Makarov, Curvilinear magnetic shells, in *Curvilinear Micromagnetism*, edited by D. Makarov and D. Sheka (Springer Nature Switzerland, 2022), Vol. 146.

[42] D. D. Sheka, Curvilinear magnetism, in *Encyclopedia of Materials: Electronics* (Elsevier, Amsterdam, 2023), pp. 760–776.

[43] D. D. Sheka, O. V. Pylypovskyi, P. Landeros, Y. Gaididei, A. Kákay, and D. Makarov, Nonlocal chiral symmetry breaking in curvilinear magnetic shells, Commun. Phys. **3**, 128 (2020).

[44] D. D. Sheka, A perspective on curvilinear magnetism, Appl. Phys. Lett. **118**, 230502 (2021).

[45] X. Huo and Y. Liu, The stability of a skyrmion in a nanotube, New J. Phys. **21**, 093024 (2019).

[46] X. Wang, X. S. Wang, C. Wang, H. Yang, Y. Cao, and P. Yan, Current-induced skyrmion motion on magnetic nanotubes, J. Phys. D **52**, 225001 (2019).

[47] D. Galvez, M. Castro, G. Bittencourt, V. Carvalho, and S. Allende, Magnetic bimerons in cylindrical nanotubes, Nanomaterials **13**, 2841 (2023).

[48] M. P. Proenca, C. T. Sousa, J. Ventura, and J. P. Araújo, Cylindrical magnetic nanotubes: Synthesis, magnetism and applications, in *Magnetic Nano- and Microwires* (Woodhead Publishing, Sawston, Cambridge, 2020) pp. 135–184.

[49] R. Streubel, E. Y. Tsymbal, and P. Fischer, Magnetism in curved geometries, J. Appl. Phys. **129**, 210902 (2021).

[50] Edited by D. Makarov and D. Sheka, *Curvilinear Micromagnetism: From Fundamentals to Applications*, Topics in Applied Physics Vol. 146 (Springer International Publishing, Cham, Switzerland, 2022).

[51] N. L. Schryer and L. R. Walker, The motion of 180° domain walls in uniform dc magnetic fields, J. Appl. Phys. **45**, 5406 (1974).

[52] M. Yan, A. Kákay, C. Andreas, and R. Hertel, Spin-Cherenkov effect and magnonic Mach cones, Phys. Rev. B **88**, 220412(R) (2013).

[53] J. A. Otálora, M. Yan, H. Schultheiss, R. Hertel, and A. Kákay, Curvature-induced asymmetric spin-wave dispersion, Phys. Rev. Lett. **117**, 227203 (2016).

[54] F. Brevis, P. Landeros, J. Lindner, A. Kákay, and L. Körber, Curvature-induced parity loss and hybridization of magnons: Exploring the connection of flat and tubular magnetic shells, Phys. Rev. B **110**, 134428 (2024).

[55] O. M. Volkov, D. D. Sheka, Y. Gaididei, V. P. Kravchuk, U. K. Rößler, J. Fassbender, and D. Makarov, Mesoscale Dzyaloshinskii-Moriya interaction: Geometrical tailoring of the magnetochirality, Sci. Rep. **8**, 866 (2018).

[56] K. V. Yershov, V. P. Kravchuk, D. D. Sheka, and U. K. Rößler, Curvature effects on phase transitions in chiral magnets, SciPost Phys. **9**, 043 (2020).

[57] Y. Liu, N. Cai, X. Yu, and S. Xuan, Nucleation and stability of skyrmions in three-dimensional chiral nanostructures, Sci. Rep. **10**, 21717 (2020).

[58] M. Zimmermann, T. N. G. Meier, F. Dirnberger, A. Kákay, M. Decker, S. Wintz, S. Finizio, E. Josten, J. Raabe, M. Kronseder *et al.*, Origin and manipulation of stable vortex ground states in permalloy nanotubes, Nano Lett. **18**, 2828 (2018).

[59] D. Cortés-Ortuño and P. Landeros, Influence of the Dzyaloshinskii-Moriya interaction on the spin-wave spectra of thin films, J. Phys.: Condens. Matter **25**, 156001 (2013).

[60] A. N. Bogdanov and U. K. Rößler, Chiral symmetry breaking in magnetic thin films and multilayers, Phys. Rev. Lett. **87**, 037203 (2001).

[61] H. Yang, A. Thiaville, S. Rohart, A. Fert, and M. Chshiev, Anatomy of Dzyaloshinskii-Moriya interaction at Co/Pt interfaces, Phys. Rev. Lett. **115**, 267210 (2015).

[62] G. D. Fratta, C. B. Muratov, F. N. Rybakov, and V. V. Slastikov, Variational principles of micromagnetics revisited, SIAM J. Math. Anal. **52**, 3580 (2020).

[63] O. M. Volkov, D. Wolf, O. V. Pylypovskyi, A. Kákay, D. D. Sheka, B. Büchner, J. Fassbender, A. Lubk, and D. Makarov, Chirality coupling in topological magnetic textures with multiple magnetochiral parameters, Nat. Commun. **14**, 1491 (2023).

[64] R. V. Kohn and V. V. Slastikov, Another thin-film limit of micromagnetics, Arch. Ration. Mech. Anal. **178**, 227 (2005).

[65] S. Rohart and A. Thiaville, Skyrmion confinement in ultrathin film nanostructures in the presence of Dzyaloshinskii-Moriya interaction, Phys. Rev. B **88**, 184422 (2013).

[66] J. C. Slonczewski, Dynamics of magnetic domain walls, AIP Conf. Proc. **5**, 170 (1972).

[67] Edited by B. Hillebrands and A. Thiaville, *Spin Dynamics in Confined Magnetic Structures III*, Topics in Applied Physics, Vol. 101 (Springer, Berlin, 2006).

[68] See Supplemental Material at http://link.aps.org/supplemental/10.1103/PhysRevB.111.184419 for videos of DW motion in different regimes and details about the OOMMF extension.

[69] B. Van Waeyenberge, A. Puzic, H. Stoll, K. W. Chou, T. Tyliszczak, R. Hertel, M. Fähnle, H. Bruckl, K. Rott, G. Reiss *et al.*, Magnetic vortex core reversal by excitation with short bursts of an alternating field, Nature (London) **444**, 461 (2006).

[70] Y. Gaididei, V. P. Kravchuk, D. D. Sheka, and F. G. Mertens, Multiple vortex-antivortex pair generation in magnetic nanodots, Phys. Rev. B **81**, 094431 (2010).

[71] M. Abramowitz and I. A. Stegun, *Handbook of Mathematical Functions with Formulas, Graphs, and Mathematical Tables*, Ninth Dover printing, Tenth GPO printing ed. (Dover Publishing, New York, 1972).

[72] D. D. Sheka, V. P. Kravchuk, and Y. Gaididei, Curvature effects in statics and dynamics of low dimensional magnets, J. Phys. A: Math. Theor. **48**, 125202 (2015).

[73] M. J. Donahue and D. Porter, The Object Oriented MicroMagnetic Framework (OOMMF), NIST (2006), https://math.nist.gov/oommf/.

[74] D. Cortés-Ortuño, M. Beg, V. Nehruji, R. A. Pepper, and H. Fangohr, OOMMF extension: Dzyaloshinskii-Moriya interaction (DMI) for crystallographic classes T and O, Zenodo (2018), doi: 10.5281/zenodo.1196820.

[75] D. Cortés-Ortuño, M. Beg, V. Nehruji, L. Breth, R. Pepper, T. Kluyver, G. Downing, T. Hesjedal, P. Hatton, T. Lancaster *et al.*, Proposal for a micromagnetic standard problem for materials with Dzyaloshinskii–Moriya interaction, New J. Phys. **20**, 113015 (2018).

[76] We were limited in computational facilities for dynamic problems.